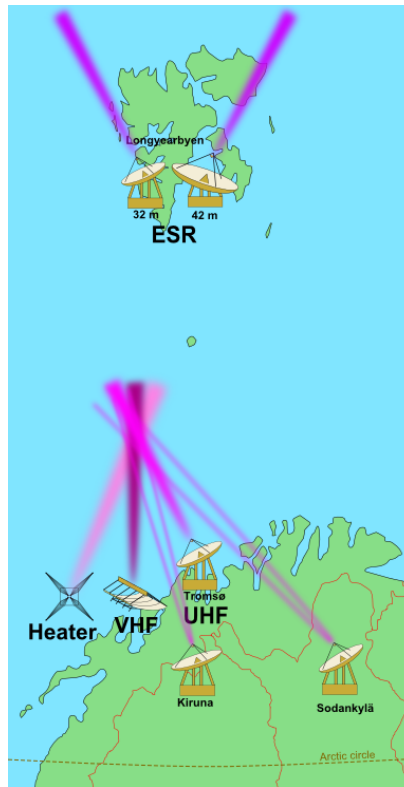


EISCAT

EUROPEAN INCOHERENT SCATTER
SCIENTIFIC ASSOCIATION

ANNUAL REPORT 2010

DRAFT COPY, November 2011



EISCAT Radar Systems

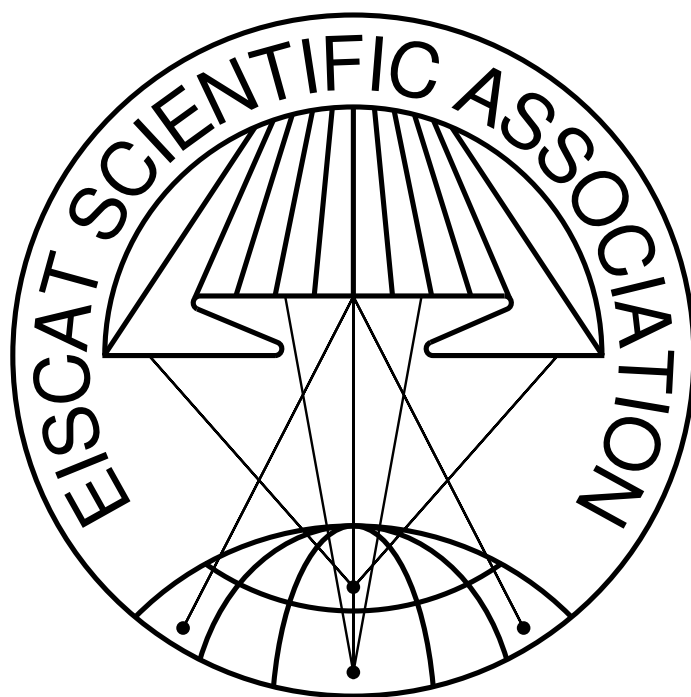
Location	Tromsø		Kiruna	Sodankylä	Longyearbyen	
Geographic coordinates	69°35'N 19°14'E		67°52'N 20°26'E	67°22'N 26°38'E	78°09'N 16°01'E	
Geomagnetic inclination	77°30'N		76°48'N	76°43'N	82°06'N	
Invariant latitude	66°12'N		64°27'N	63°34'N	75°18'N	
Band	VHF	UHF	UHF	UHF	UHF	
Frequency (MHz)	224	931	931	931	500	
Maximum bandwidth (MHz)	3	8	8	8	10	
Transmitter	1 klystron	2 klystrons	-	-	16 klystrons	
Channels	8	8	8	8	6	
Peak Power (MW)	1.6	2.0	-	-	1.0	
Average power (MW)	0.20	0.25	-	-	0.25	
Pulse duration (ms)	0.001–2.0	0.001–2.0	-	-	0.0005–2.0	
Phase coding	binary	binary	binary	binary	binary	
Minimum interpulse (ms)	1.0	1.0	-	-	0.1	
Receiver	analog	analog	analog	analog	analog	
System temperature (K)	250–300	90–110	50	50	65–80	
Digital processing	14 bit ADC, 32 bit complex, autocorrelation functions, parallel channels				12 bit ADC, lag profiles 32 bit complex	
Antenna	parabolic cylinder 120 m × 40 m steerable	parabolic dish 32 m steerable	parabolic dish 32 m steerable	parabolic dish 32 m steerable	Antenna 1 parabolic dish 32 m steerable	Antenna 2 parabolic dish 42 m fixed
Feed system	line feed 128 crossed dipoles	Cassegrain	Cassegrain	Cassegrain	Cassegrain	Cassegrain
Gain (dBi)	46	48.1	48.1	48.1	42.5	44.8
Polarisation	circular	circular	any	any	circular	circular

EISCAT Heating Facility in Tromsø

Frequency range: 4.0–8.0 MHz, Maximum transmitter power: 12×0.1 MW, Antennas: Array 1 (5.5–8.0 MHz) 30 dBi, Array 2 (4.0–5.5 MHz) 24 dBi, Array 3 (5.5–8.0 MHz) 24dBi.

Additionally, a Dynasonde is operated at the heating facility.

Cover picture: Solar activity dependence of ion upflow in the polar ionosphere,
from the article by Y. Ogawa et al. (2010).



EISCAT Scientific Association
2010

EISCAT, the European Incoherent Scatter Scientific Association, is established to conduct research on the lower, middle and upper atmosphere and the ionosphere using the incoherent scatter radar technique. This technique is the most powerful ground-based tool for these research applications. EISCAT is also being used as a coherent scatter radar for studying instabilities in the ionosphere, investigating the structure and dynamics of the middle atmosphere, studying meteors and as a diagnostic instrument in ionospheric modification experiments with the heating facility.

There are fourteen incoherent scatter radars in the world, and EISCAT operates three of the highest-standard facilities. The EISCAT sites are located north of the Arctic Circle in Scandinavia. They consist of two independent radar systems on the mainland, together with a radar constructed on the island of Spitzbergen in the Svalbard archipelago — the EISCAT Svalbard Radar (see sketch and operating parameters on the inside of the front cover).

The EISCAT UHF radar operates in the 931 MHz band with a peak transmitter power of 2.0 MW, and employs fully steerable 32 m parabolic dish antennas. The transmitter for this system and one of the receivers are located in Tromsø (Norway). Receiving sites are also located in Kiruna (Sweden) and Sodankylä (Finland), allowing for tri-static radar measurements.

The monostatic VHF radar in Tromsø operates in the 224 MHz band with a peak transmitter power of 1.6 MW, using a 120 m × 40 m parabolic cylinder antenna which is subdivided into four sectors. This antenna can be steered mechanically in the meridional plane from vertical to 60° north of the zenith; limited east-west steering is also possible using alternative phasing cables.

The EISCAT Svalbard radar (ESR), located near Longyearbyen, operates in the 500 MHz band with a peak transmitter power of 1.0 MW, and employs a fully steerable parabolic dish antenna of 32 m diameter and a fixed antenna, aligned with the local magnetic field, with a 42 m diameter. The high latitude location of this facility is particularly aimed at studies of the cusp and the polar cap region.

The basic data measured with the incoherent scatter radar technique are profiles of electron density, electron and ion temperatures and bulk ion velocity. Subsequent processing allows derivation of a wealth of further parameters, describing the ionosphere and neutral atmosphere. A selection of well-designed radar pulse schemes are available to adapt the data-taking routines to many particular phenomena, occurring at altitudes from about 50 km to above 2000 km. Depending on geophysical conditions, a best time resolution of less than one second and an altitude resolution of a few hundred meters can be achieved.

Operations of 3000–4000 hours each year are distributed between Common Programmes (CP) and Special Programmes (SP). At present, six well-defined Common Programmes are run regularly, for between one and three days, typically about once per month, to provide a data base for long term synoptic studies. A large number of Special Programmes, defined individually by Associate scientists, are run to support national and international studies of both local and global geophysical phenomena.

Further details of the EISCAT system and its operation can be found in various EISCAT reports, including illustrated brochures, which can be obtained from EISCAT Headquarters in Kiruna, Sweden.

The investments and operational costs of EISCAT are shared between:

*China Research Institute of Radiowave Propagation, Peoples Republic of China
Deutsche Forschungsgemeinschaft, Germany
National Institute of Polar Research, Japan
Natural Environment Research Council, United Kingdom
Norges forskningsråd, Norway
Solar-Terrestrial Environment Laboratory, Nagoya University, Japan
Suomen Akatemia, Finland
Vetenskapsrådet, Sweden*

Contents

The Council Chairperson’s section	7
EISCAT_3D	8
Scientific highlights 2010	10
Mesospheric studies	10
Spectral widths of polar mesospheric summer echoes	10
Study of layered dusty plasma structures in the summer polar mesopause	11
Polar mesosphere winter echoes	12
Thermospheric studies	13
Tidal waves in the polar lower thermosphere	13
SCANDI, an all-sky Doppler imager for studies of thermospheric spatial structure	13
Lower-thermospheric wind fluctuations	14
Ionospheric studies	15
Solar activity dependence of ion upflow in the polar ionosphere	15
EISCAT observation of quiet-time ionospheric trough	15
Spectrally uniform scattering cross section enhancements and ion-acoustic solitary waves	16
Enhanced ion acoustic line in the high ionosphere	17
Statistical investigation of the Cowling channel efficiency in the auroral zone	17
Comparison of EISCAT and SuperDARN F-region measurements	18
Polar cap studies	19
Multi-radar study of global polar cap patch dynamics and morphology	19
Seasonal influence on polar cap patches in the high-latitude nightside ionosphere	19
Observations of polar cap patches with the ESR and rockets	20
The open-closed field line boundary	20
Polar cap boundary location using IMAGE and EISCAT	21
Polar cap signatures	22
Studies of particle precipitation and the aurora	23
Determination of the characteristic energy of precipitating electrons	23
Acceleration mechanism for flickering aurora	23
Studies of dust and meteorites	23
ECOMA sounding rocket campaign	23
Solar wind studies	24
Interplanetary scintillation observations	24
Studies of fundamental plasma physics	27
Ray tracing analysis of L mode pumping of the ionosphere	27
Observations of heating experiments in the low ionosphere in polar winter	27
Activities by the Arctic and Antarctic Research Institute (AARI) in 2010	28
UK studies involving artificial heating	31
Inversion results of incoherent scatter spectra	34
Spectra of non-Maxwellian distributions	35
New radar techniques	35
Simulation of post-ADC digital beamforming for large aperture array radars	35

List of publications 2010	37
EISCAT Operations 2010	40
List of meetings 2010	44
Staff celebrations 2010	45
Beynon medals	46
EISCAT organisational diagram 2010	47
Committee Membership and Senior Staff	48
Appendix: EISCAT Scientific Association Annual Report, 2010	51
The EISCAT Associates, December 2010	65
Contact Information	66

The Council Chairperson's section

In summer 2010 EISCAT started to gradually lose its unique capability of tri-static measurements as the frequency band used for the UHF-radars was given to mobile phone operators in Lapland. The demand from the science community still continued to be high for the all EISCAT facilities and therefore an important challenge for the Council was to make wise decisions for ensuring continued operations with the aging instrumentation.

The acceptance of EISCAT_3D to the ESFRI roadmap was an important factor to open new opportunities for additional EU funding for the EISCAT_3D mission. The new Director of EISCAT, Dr. Esa Turunen, together with Dr. Ian McCrea made the valuable work to harvest these opportunities. They collected a group of experienced EISCAT scientists who prepared a successful proposal to the EU FP7 call dedicated to research infrastructure preparatory phase activities. The EISCAT_3D Preparatory Phase (PP) started in autumn 2010. The consortium conducting the PP work is led by EISCAT and it includes research institutes from the host countries of the current EISCAT facilities and from the UK. Since the beginning of the project, its progress reports have been one the most interesting items in the Council meetings' Agenda.

It is obvious that EISCAT_3D-PP gives positive momentum also to the current EISCAT activities. Therefore, I hereby want to express Council's warm acknowledgements to the EISCAT Executives and other partners in the PP consortium for their efforts in EISCAT_3D development. Having said this, however, I want to remind that although not all the current EISCAT member countries are involved directly in the PP-activities, the EISCAT_3D mission will be a success only if the whole Association joins the effort. The future EISCAT activities will get funding only if they are supported by a multinational science community which has the urge to make good science with the combination of EISCAT_3D and ESR. In parallel with the PP work, it will be important to pay attention also to the development of the ESR system. Svalbard measurements will have a crucial role in

maintaining the scientific interest towards EISCAT during the years when the mainland radars are renovated. Therefore, the Council was glad to notice that the mission of China to extend the ESR system with a third antenna started to take the first steps from a proposal towards a concrete working plan in 2010.

Economically difficult times in the Association continued during 2009–2010 and the uncertain conditions are likely to continue at least for some more years. As a consequence from this situation the working environment may not have been optimal in all respects for the EISCAT Staff. Despite of the challenging situation these people have shown excellent performance both in conducting the EISCAT standard operations and in EU project work. On behalf of the EISCAT Council I want to thank the Staff members for taking care of the primary business of the Association, i.e. maintaining the most versatile ISR system in the world. I'm sure that the whole EISCAT research community is ready to join in these acknowledgements. The Director of EISCAT has done excellent work in advertising EISCAT_3D in several different forums. He has also been a key person in the implementation of the new EISCAT peer-review program, where scientists from all countries, both inside and outside EISCAT, can make proposals for new innovative EISCAT experiments. I have no difficulties to believe that his persistent and enthusiastic PR work will eventually attract some new user groups for EISCAT and this way improve also the economical situation of the Association.

The two year period as the Council Chairperson has been very rewarding time for me. Collaboration inside the Council, with the EISCAT Executives and with national funding agencies has been fluent and a very teaching experience. Therefore, I wish to thank all those people with whom I have been working in EISCAT business during the Chairperson period.

*Dr. Kirsti Kauristie
Chairperson, EISCAT Council*

EISCAT_3D

On 30 April 2009, the four-year EISCAT_3D Design Study was completed. It was supported by the Sixth Framework Programme of the European Union. The goals of the Design Study were to study the feasibility of constructing a third generation incoherent scatter research radar, that would be using cutting-edge technology throughout, in order to provide an order-of-magnitude improvement in the temporal and spatial resolution when replacing the existing aging EISCAT VHF and UHF systems — and to produce a detailed design for such a system. This was reported in the EISCAT Annual Report 2009.

The next stage of the development of the EISCAT_3D project is the Preparatory Phase. In the Preparatory Phase the aim is to ensure that the EISCAT_3D project will reach a sufficient level of maturity with respect to technical, legal and financial issues so that it will be possible to begin construction of the EISCAT_3D radar system. Thanks to the inclusion of the EISCAT_3D project on the ESFRI Roadmap for Research Infrastructures in 2008, it was possible to apply for EU funding for the Preparatory Phase through EU Framework Programme 7, under the call FP7-INFRASTRUCTURES-2010-1 (Construction of new infrastructures: providing catalytic and leveraging support for the construction of new research infrastructures). The funding application for the Preparatory Phase was submitted to the EU system in early December 2009. The plan was for 48 months of work, and an amount of 6 M€ was requested. Later, during the negotiations in June 2010, the budget was adjusted down to a requested amount of 4.5 M€ from

the European Commission in order for the EISCAT_3D Preparatory Phase project to be accepted. Thus, the work in the EISCAT_3D Preparatory Phase could start in October 2010.

The workplan for the EISCAT_3D Preparatory Phase is divided into fourteen individual Work Packages that are intended to cover the areas intended to be targeted by the Preparatory Phase. The Work Packages are:

- WP1** Project management and reporting
- WP2** Legal and logistical issues
- WP3** Science planning and user engagement
- WP4** Outreach activities
- WP5** Consortium building
- WP6** Performance specification
- WP7** Digital signal processing
- WP8** Antenna, front end and time synchronisation
- WP9** Transmitter development
- WP10** Aperture synthesis imaging radar
- WP11** Software theory and implementation
- WP12** System control
- WP13** Data handling and distribution
- WP14** Mass production and reliability

The consortium involved in the EISCAT_3D Preparatory Phase work includes eight partners. These are EISCAT Scientific Association, University of Oulu (including Sodankylä Geophysical Observatory), Luleå Technical University, Swedish Institute of Space Physics, University of Tromsø, STFC-RAL, National Instruments and the Swedish Research Council (including Swedish National Infrastructure for Computing).

The EISCAT_3D Preparatory Phase started formally on 1 October 2010, and the first EISCAT_3D General Assembly meeting was held on





Artist's vision of the core EISCAT_3D antenna field.

6 October 2010. The General Assembly is the decision-making body of the EISCAT_3D Preparatory Phase consortium and it consists of one representative from each of the participating partners (two from the Coordinator, i.e. EISCAT). The members of the General Assembly are Esa Turunen (EISCAT), Henrik Andersson (EISCAT), Cesar La Hoz (University of Tromsø), Jerker Delsing (Luleå Technical University), Lars Eliasson (Swedish Institute of Space Physics), Anita Aikio (University of Oulu), Tomas Andersson (Swedish Research Council), Leif Johansson (National Instruments) and Richard Harrison (STFC).

One of the items at the first General Assembly meeting was to decide the members of the EISCAT_3D Executive Board, which is the supervisory body for the execution of the EISCAT_3D Preparatory Phase. It was decided that the Executive Board would consist of Esa Turunen, Henrik Andersson, Jonny Johansson (Luleå Technical University), Thomas Ulich (University of Oulu), and Ian McCrea (STFC) with Anders Tjulin (EISCAT) also attending the meetings. The Executive Board has weekly tele-conferences, and also meet physically once every three months.

A kick-off meeting for the EISCAT_3D Preparatory Phase was held 21–22 October 2010 at Clarion Hotel Stockholm. Representatives from all Work Packages and all Project Partner institutes were present, as well as representatives from the European Commission and other people interested in the EISCAT_3D development. The three main themes that was discussed during the meeting were public engagement, support activities

and the specific EISCAT_3D Preparatory Phase actions. The 21 presentations at the meeting gave a good overview of the status within these themes.

The final three months of 2010 were also the first three months of the EISCAT_3D Preparatory Phase. The focus during these months were to start up get the project going. An example of the progress in the project during these months are the establishment of the initial Science Working Group, a group that combines existing EISCAT users with members of other science communities so that during the lifetime of the EISCAT_3D Preparatory Phase it will be possible to cover all of the EISCAT_3D related science themes. Another example of early progress in the project is the launch of the upgraded EISCAT_3D project web-site.

Outside of the EISCAT_3D Preparatory Phase, the second EISCAT_3D Users Meeting was held 19–21 May, 2010, at Ångström Laboratory in Uppsala, Sweden, following the success of the first Users Meeting at the same location one year earlier. This was an open meeting for the prospective users of the future EISCAT_3D facility. The meeting was organised as a two-way communication exercise, where the plans for the EISCAT_3D Preparatory Phase activities were presented to the user community and the user community's scientific requirements for the system were gathered. In total 36 presentations on EISCAT_3D related topics were presented, and it was decided to continue having EISCAT_3D Users Meetings in Uppsala in May.

*Dr. Anders Tjulin
Project Assistant, EISCAT Scientific Association*

Scientific highlights 2010

Mesospheric studies

Spectral widths of polar mesospheric summer echoes

A controversial discussion in the literature about the agreement or disagreement of spectral widths (after conversion to Doppler-velocities) of Polar Mesospheric Summer Echoes (PMSEs) observed simultaneously with the EISCAT VHF and UHF radars motivated a detailed investigation of this topic. A much larger data set than in any of the previous studies has been analysed. The previous discussions only considered case studies of a few minutes in length, whereas Strelnikova and Rapp (2011) considered a total of 380 min (in total 760 samples) of simultaneous and common volume observations with these two radars. In that study it is discussed whether PMSEs at these two frequencies originate from the same coherent scattering mechanism or if different physical mechanisms are necessary to explain these echoes. Both the shape and the width of the considered spectra were investigated and it was found that (within the available spectral resolution) the VHF spectra are on average well described by a Gaussian shape (with spectral parameter $n = 2$), which is derived from a generalised formulation of the autocorrelation function, whereas the UHF-spectra show a small deviation from this shape.

Figure 1 indicates that the spectral widths do largely agree, but show a small systematic difference which can be explained by considering the effect of beam-, shear-, and wave-broadening. This means that the slightly different beam widths of the VHF and UHF radars and the hence slightly different illuminated volumes account for the small systematic difference in mean spectral width. Finally, it was demonstrated that the small deviation of the UHF-spectra from a perfect Gaussian shape can be either due to relatively small signal-to-noise ratios of the UHF-data and/or a superposition of incoherent and coherent scatter in cases where both contributions add equally to the

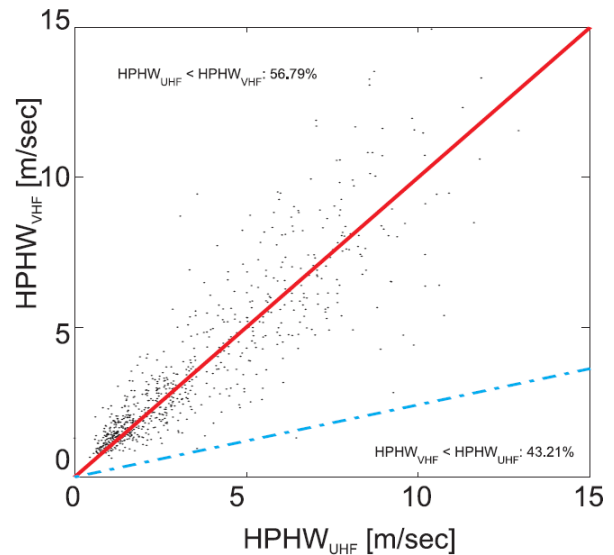


Figure 1: Half width at half maximum measured simultaneously with the UHF and VHF radars. The red solid line shows a 1:1 slope. The blue dash-dotted line shows the relationship of two spectral widths as expected in the case of an incoherent scatter mechanism.

total observed power. Since VHF PMSEs are much stronger than the incoherent scatter background, this effect cannot be recognized in VHF observations. This superposition effect may occasionally also lead to larger deviations between VHF and UHF spectra and, hence, significantly narrower UHF spectra. However, excluding these rather rare and exotic cases, Strelnikova and Rapp (2011) concluded that the majority of the observations are compatible with a single coherent scattering at both VHF and UHF.

Vertical wind fluctuations have been investigated to discuss the contributions of atmospheric wave activity on the spectral width. Figure 2 demonstrates that these fluctuations are modulated periodically. From the power spectrum of the modulation a dominant period (~ 13 min in this case) can be identified. The wave periods for EISCAT VHF radar estimates of vertical wind fluctuations are summarised in Fig. 3 where time peri-

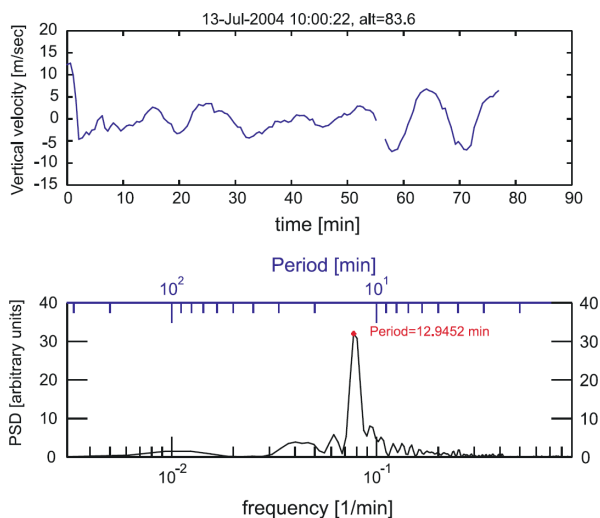


Figure 2: Example of vertical wind measurement and spectrum of wind fluctuations. This example was taken on 13 July 2004 from 10:00 to 11:20 UT at an altitude of 83.6 km.

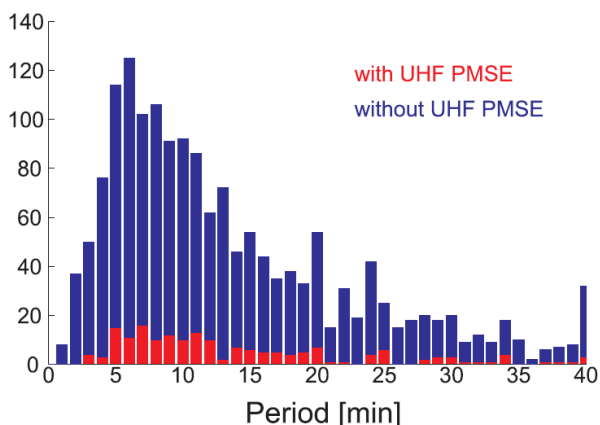


Figure 3: Histogram of wave periods derived from the spectral analysis of vertical wind observations obtained from VHF PMSE data. The blue histogram shows the results for all VHF PMSE observations in July 2004 and 2005 and the red histogram shows the subset of data where UHF PMSE were observed simultaneously.

ods where PMSEs also occurred in the UHF radar measurements are separated from periods where they did not. Both distributions show a maximum of wave periods in the order of 5–10 min.

I. Strelnikova, and M. Rapp, “Majority of PMSE spectral widths at UHF and VHF are compatible with a single scattering mechanism”, *J. Atmos. Solar-Terr. Phys.*, doi:10.1016/j.jastp.2010.11.025, in press, 2011.

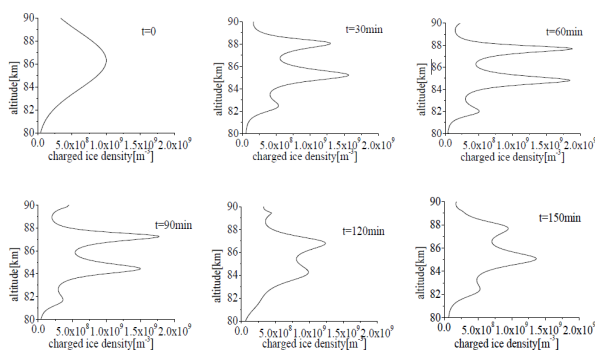


Figure 4: Evolution of number density profiles due to gravity wave modulation. The time interval between each panel is 30 min ($t = 0, 30, 60, 90, 120, 150$ min), with the vertical wavelength of 3 km for the gravity waves and an intrinsic period of 2 hours.

Study of layered dusty plasma structures in the summer polar mesopause

Data from sounding rocket campaigns indicate that the radar Signal to Noise Ratio (SNR), the electron density and the dust charge density of the summer polar mesosphere have obvious layered structure.

Traditional hydrodynamic equations are adapted to build a one-dimensional theoretical model to study the effect of gravity waves on the formation and evolution of layered dusty plasma structures near the polar summer mesopause region that is associated with the Polar Mesosphere Summer Echoes (PMSEs). The proposed mechanism puts emphasis on the charged ice particle motion by gravity wave modulation, making a significant contribution to the vertically transport of heavy ice particle and convergence into thin layers. Figure 4 shows how a charged ice particle distribution with an initial Gaussian shape transforms into distinct thin-layer structures.

As shown by Figs. 5 and 6, the pattern of the multi-layer structure depends on the vertical wavelength of the gravity waves and on the size of the ice particles. Based on the above mechanism, with the vertical wavelength 2.5 km and the period 4 hours, the experimental result recorded during the ECT02 sounding rocket campaign (Havnes et al., 1996) was reproduced as shown in Figure 7.

In addition, based on the theory of wave propagation in layered media, SNR in polar mesosphere during PMSEs were studied. By comparing the calculated and experimental results (Fig. 8), the calculated SNR almost agrees with the exper-

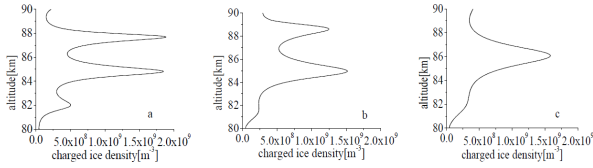


Figure 5: The influence from the vertical wavelength of the gravity waves on the formation of ice particle layers. The wavelengths are $\lambda = 3$ km, 4 km and 5 km respectively.

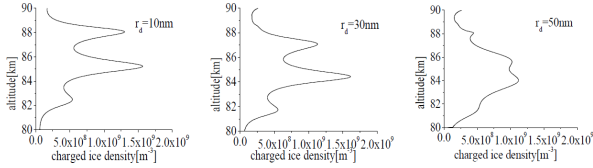


Figure 6: The effect on the formation of layer structures from different ice particle sizes. The sizes are $r_d = 10$ nm, 30 nm and 50 nm respectively.

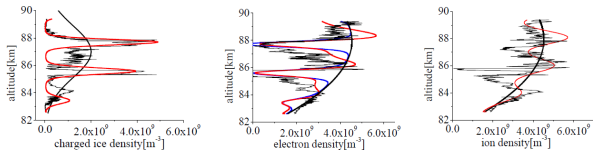


Figure 7: Comparison between the ECT02 rocket sounding data (thin black line) and the model calculations results (red line). The estimated vertical wavelength is 2.5 km and the period is 4 hours.

imental one, but there are still some differences between the calculated and the experimental results, which may be caused by the vacuum assumption at altitude 0–83 km and the neglected possible effects from the magnetic field. In fact, the magnetic field should not have any important impact in the VHF and UHF bands, but when the observation are carried out in the MF and HF bands the influence of magnetic field should be taken into account.

H. Li, et al., “Study on the layered dusty plasma structures in the summer polar mesopause”, *Ann. Geophys.* 28, 1679–1686, 2010.

H. Li, et al., “Reflection characteristics of layered media in polar mesopause occurring polar mesosphere summer echoes”, *Plasma Science and Technology* 12, 2010.

Polar mesosphere winter echoes

Polar Mesosphere Winter Echoes (PMWEs) have been analysed in great detail and the first results have been presented (e.g. Engler et al., 2010a,b). Figure 9 shows the statistics of the spectral shape

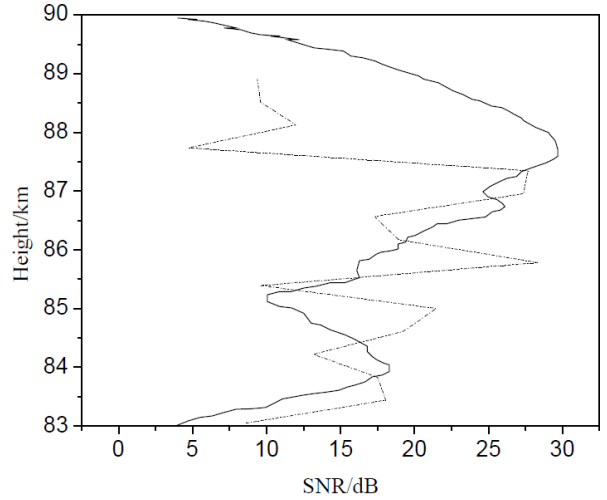


Figure 8: Profile of the SNR measured with the ALOMAR-SOUSY VHF radar during sounding rocket flight ECT02 (solid line). Profiles of SNR calculated with the method of layered media (dashed line).

determined by fitting the auto-correlation functions using the algorithm discussed by Strelnikova and Rapp (2010). Several models have been proposed in the literature (e.g. turbulence or damped viscosity waves) to explain these radar echoes occurring at lower mesospheric altitudes than mesospheric summer echoes. Extracting the n parameters only for strong echoes show that inside the strong PMWE the n parameters are similar to 2 which exhibits a Gaussian spectral shape. The analysis of the spectral shape supports the theory that turbulence is an important mechanism for the occurrence of PMWEs. On the other hand, the radar echoes observed with the EISCAT VHF radar are too strong to be explained by turbulence alone because extremely high turbulence activity would have been necessary to achieve such strong echoes as those observed. Additional contributions have to be considered to explain the physical mechanism responsible for the occurrence of PMWEs.

N. Engler, M. Rapp, and I. Strelnikova, “Analysis of the spectral form of polar mesosphere winter echoes measured with the eiscat-vhf-radar”, Talk at DPG Frühjahrstagung, Bonn, Germany, March 15–19, 2010a.

N. Engler, M. Rapp, and I. Strelnikova, “Analysis of polar mesosphere winter echoes using the EISCAT-VHF-radar”, Poster at SCOSTEP-12 Symposium, Berlin, Germany, July 12–16, 2010b.

I. Strelnikova, and M. Rapp (2010), “Studies of polar mesosphere summer echoes with the EISCAT

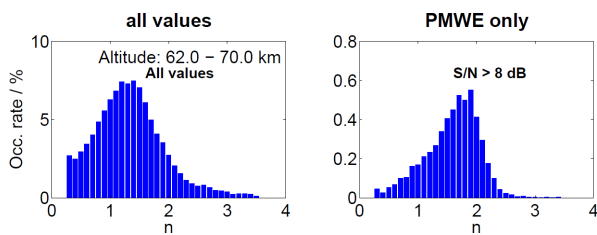


Figure 9: Statistical analysis of the spectral form of PMWEs. The majority of the observations show a Lorentzian shape while inside strong PMWEs the Gaussian shape dominates.

VHF and UHF radars: Information contained in the spectral shape”, *Adv. Space Res.* 45, 247–259, doi:10.1016/j.asr.2009.09.007.

Thermospheric studies

Tidal waves in the polar lower thermosphere

Characteristics of the lower thermospheric wind have been determined from a long run data set obtained by the EISCAT UHF radar at Tromsø (69.6°N, 19.2°E) over ~23 days, from September 6 to 29, 2005 (Fig. 10). The derived semidiurnal amplitude exhibited day-to-day variations (~5–30 m/s) at and above 109 km, while the phase varied little with the day. A mode change was found of the semidiurnal tide occurring during September 17–22, 2005. Between September 6 and 16 the vertical wavelengths were estimated to be ~58 km and ~76 km for the meridional and zonal components, respectively, while between September 23 and 29 they became less than ~24 km. Wind data from MF radars co-located at Tromsø, and also at Poker Flat, were also analysed. Comparison of the wind data from the two MF radars indicated that migrating semidiurnal tide was dominating in the mesosphere. Furthermore, the vertical wavelengths (i.e., modes) were different to each other in the mesosphere and the lower thermosphere for each interval. The day-to-day variability of the diurnal tide was less obvious than that of the semidiurnal tide. The diurnal amplitude of the meridional component increased with height except for 8 days between September 13 and 20, when the diurnal amplitudes had smaller values (< 40 m/s) at and above 111 km than for the other intervals. Furthermore, the shapes of the altitude profiles of the meridional phase differ from those for the other intervals. Contributions due to the electric field and the ion drag acceleration were

evaluated, and it was shown that they were not causing this. From the analysis of 22.5 days of wind data, about 5–6 day oscillations were found in the lower thermosphere, probably where there were planetary wave activity in the lower thermosphere.

S. Nozawa, et al., “Tidal waves in the polar lower thermosphere observed using the EISCAT long run data set obtained in September 2005”, *J. Geophys. Res.* 115, A08312, doi:10.1029/2009JA015237, 2010.

SCANDI, an all-sky Doppler imager for studies of thermospheric spatial structure

Aruliah et al. (2010) has presented the initial results from a new all-sky Fabry-Perot Interferometer (FPI) called the Scanning Doppler Imager (SCANDI), which has been built and installed at Longyearbyen, Svalbard, and was first operated in December 2006. SCANDI observes the Doppler shifts and Doppler broadening of the 630 nm airglow and aurora from which upper thermospheric winds and temperatures can be calculated. The imager allows measurements over a field-of-view (FOV) with a horizontal radius of nearly 600 km for observations at an altitude of 250 km, using a time resolution of 8 minutes. SCANDI provides the ability to observe thermospheric spatial structure within a FOV which overlaps the FOVs of the EISCAT Svalbard radar and CUTLASS SuperD-ARN radars. Coordination with these instruments provides an important opportunity for studying ion-neutral coupling. The all-sky image is divided into several sectors to provide a horizontal spatial resolution of between 100 and 300 km. The new instrument represents a powerful extension in observational capability but it requires careful calibration and data analysis. Two observation modes have been used: one fixed and one scanning etalon gap. SCANDI results have been corroborated using the Longyearbyen single look direction FPI, together with ESR measurements of the ion temperatures. The data reveal thermospheric temperature gradients of a few K/km and a great deal of meso-scale variability, on spatial scales of several tens of kilometres.

A. L. Aruliah, et al., “SCANDI an all-sky Doppler imager for studies of thermospheric spatial structure”, *Ann. Geophys.* 28, 549–567, 2010.

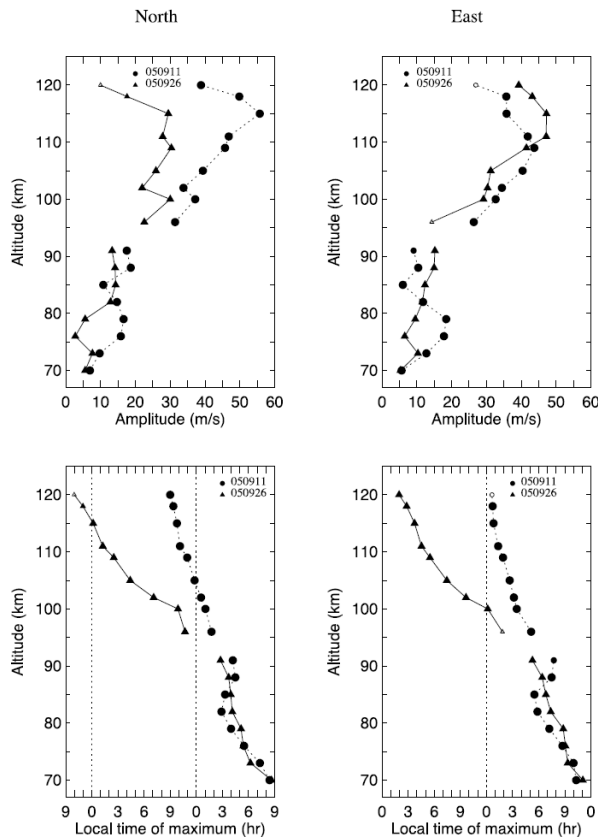


Figure 10: Altitude profiles between 70 and 120 km of the amplitudes (top panels) and the corresponding phases, i.e. the local time of maximum, (bottom panels) of the semidiurnal tides for the meridional (left panels) and the zonal (right panels) components. Circles (and dashed lines) denote results from the 10 day data window starting at 19:00 UT on September 6, while triangles (and solid lines) denote results from the 6 day data window starting at 07:00 UT on September 23. Larger filled symbols denote data above 99% significance level, smaller filled symbols denote data between 50% and 99% significance levels, and open symbols denote data below 50% significance level. EISCAT UHF data are shown for altitudes at and above 96 km, while Tromsø MF radar data are shown for altitudes at and below 91 km.

Lower-thermospheric wind fluctuations

Simultaneous observations were conducted with a Fabry-Perot Interferometer (FPI) at a wavelength of 557.7 nm, an all-sky camera at a wavelength of 557.7 nm, and the European Incoherent Scatter (EISCAT) UHF radar during the Dynamics and Energetics of the Lower Thermosphere in Aurora 2 (DELTA-2) campaign in January 2009 (Fig. 12). This study concentrates on two events during periods of pulsating aurora. The lower-

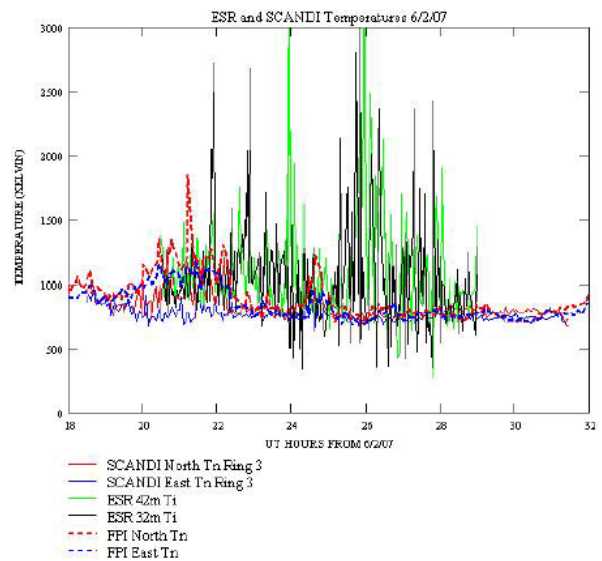


Figure 11: Comparison of ion temperatures observed by the two ESR radars with the neutral temperatures observed by SCANDI on the night of 6–7 February 2007.

thermospheric wind velocity measured with the FPI showed obvious fluctuations in both the vertical and the horizontal components. Of particular interest is that the location of the fluctuations are found in a darker area that appeared within the pulsating aurora. During the same time period the EISCAT radar observed sporadic enhancements in the F-region backscatter echo power, suggesting presence of low-energy electron (1 keV or lower) precipitation coinciding with an increase in the amplitude of the electromagnetic wave (at the order of 10 Hz or higher). While the dominant mechanism causing the fluctuations in FPI-derived wind velocity during the pulsating aurora have not yet been identified, the frictional heating energy dissipated by the electric-field perturbations may be responsible for the increase in ionospheric thermal energy and thus modifying the local wind dynamics in the lower thermosphere.

S. Oyama, et al., “Lower-thermospheric wind fluctuations measured with an FPI in pulsating aurora at Tromsø, Norway”, *Ann. Geophys.* 28, 1847–1857, 2010.

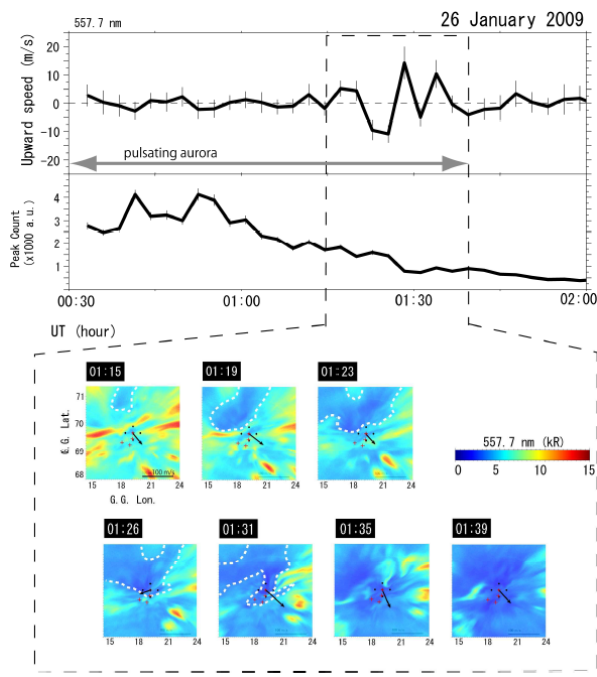


Figure 12: The top and middle panels show the temporal variations in the vertical wind speed and the fringe peak count at the zenith, respectively, measured with the FPI (557.7 nm) from 00:30 to 02:00 UT on 26 January 2009. The vertical bars denote the 2σ uncertainty. The bottom panels show horizontal aurora images taken with the ASC at 557.7 nm from 01:15 to 01:39 UT during pulsating aurora (the corresponding time interval is marked by black dashed line in the top two panels). The colour scale of the optical intensity is shown at centre right. These images are mapped in geographic coordinates assuming that the peak emission height is 110 km. The five black dots and the four red crosses indicate the location of the FPI and the EISCAT UHF radar observation positions, respectively. The black arrows correspond to the horizontal component of the FPI-derived neutral wind velocity (the scale is presented at the right bottom corner of the first panel from the left). White dashed lines are drawn in the colour panels to easily identify the darker area.

Ionospheric studies

Solar activity dependence of ion upflow in the polar ionosphere

The influence of solar activity on ion upflow in the polar ionosphere has been investigated using data obtained by the European Incoherent Scatter (EISCAT) Tromsø UHF radar between 1984 and 2008. In agreement with other work the upward ion flux was generally found to be higher at high solar

activity than at low activity. Ion upflow events, and also the upward velocity, behave the opposite: they are more frequent and at higher altitudes at times of low solar activity. In any year about 30%–40% ion upflow is accompanied by ~ 500 K higher electron temperature than the background temperature at 400 km altitude. Electron and ion heating in connection with upflow is nearly twice as prevalent during high solar activity than at low activity. The acceleration of ions by pressure gradients and ambipolar electric field becomes larger at low solar activity compared to high activity. This variation of the average acceleration is caused by the different shape of the electron density profile when the solar activity is low compared when it is high. Ions start to flow upward at above 450 km altitude at high solar activity, and lower (at 300–500 km altitude) at low solar activity. It is suggested that the solar activity influences the long-term variations of the ion upflow occurrence because it modulates the density of the neutral particles, the formation of the F2 density peak, and the ion-neutral collision frequencies in the thermosphere and ionosphere.

Y. Ogawa, et al., “Solar activity dependence of ion upflow in the polar ionosphere observed with the EISCAT Tromsø UHF radar”, *J. Geophys. Res.* 115, A07310, doi:10.1029/2009JA014766, 2010.

EISCAT observation of quiet-time ionospheric trough

Data from combined azimuth-scan and overhead-scan UHF experiments were used to determine the behaviour of the eveningside F-region trough on 9 November 1987. The MLT and CGMlat dependence of various ionospheric parameters at a set of F region altitudes was determined. It was found that both ion and electron temperatures have minima within the trough region, and increase at the poleward edge. The most important result was obtained by comparing the observed ion velocity and electron density to the respective parameters given by the LiMIE model (see Fig. 14). The results suggest that the density depletion within the trough is due to recombination of F-region plasma convecting for a long time in the dusk convection cell beyond the terminator. The northern edge of the trough is associated with soft particle precipitation. The southern edge is steeper than the northern one, and is built by sun-lit plasma brought to the trough region by co-rotation. The trough is thus a result of a combination of transport and precipitation processes rather than stagnation.

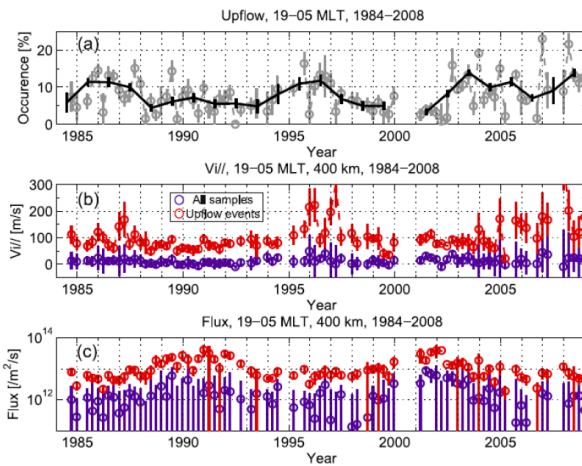


Figure 13: (a) Occurrence frequency of ion upflow starting between 200 and 550 km altitude in the nighttime between 19:00 and 05:00 MLT is shown between 1984 and 2008: 1 year average (black line) and 3 month average (gray circles). (b) Average field-aligned ion velocity at 400 km altitude versus year. Red circles indicate the average flux in upflow events, and blue circles indicate the average flux of all samples (upflow, no-flow, and downflow events). (c) Average field-aligned flux at 400 km altitude versus year. These circles are plotted every 3 months.

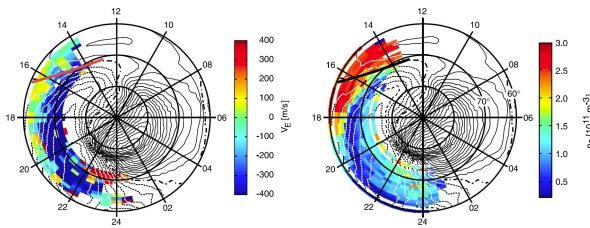


Figure 14: Zonal ion velocity (left panel) and electron density (right panel) at 345 km together with the convection pattern given by the LiMIE model. Positive potential is indicated by continuous lines and negative potential by dashed lines. The position of the solar terminator is also indicated in the plots as a line of contrasting colour.

M. Voiculescu, et al., “An olden but golden EISCAT observation of a quiet-time ionospheric trough”, *J. Geophys. Res.* 115, A10315, doi:10.1029/2010JA015557, 2010.

Spectrally uniform scattering cross section enhancements and ion-acoustic solitary waves

Spectra measured by incoherent scatter radars are formed predominantly by scattering of the incid-

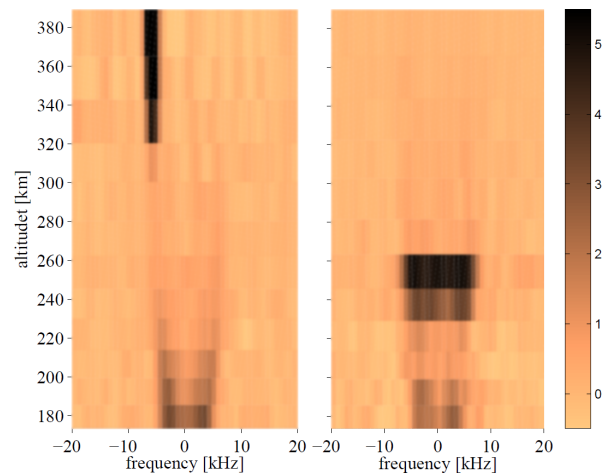


Figure 15: Incoherent radar spectra obtained with ESR. The left panel shows a typical NEIAL at altitudes above 300 km on 9 April 2007 at 11:31:54 UT. The right panel shows a different kind of spectral enhancement seen on 1 August 2007 at 00:43:00 UT. Both spectra had 6 s integration time. The colour bar shows the range corrected power spectral density in arbitrary units.

ent signal off ion-acoustic waves and Langmuir waves in the ionosphere. Occasionally, the upshifted and/or downshifted lines produced by the ion-acoustic waves are enhanced well above thermal levels and referred to as Naturally Enhanced Ion-Acoustic Lines (NEIALs; Fig. 15, left panel). At other times a different kind of enhancement is seen, which is spectrally uniform over the whole ion-line, i.e. the up- and downshifted shoulder and the spectral valley in between (Fig. 15 right panel). Based on observations made with the EISCAT Svalbard Radar (ESR) facility, the transient and spectrally uniform power enhancements were investigated and found to be explained by ion-acoustic solitary waves. A theory of nonlinear waves in a magnetised plasma enables the determination of the properties of such waves and the evaluation of their effects on the scattered signals measured by the ESR. This new mechanism can explain backscattered power enhancements by one order of magnitude above the thermal level and is consistent with observations.

J. Ekeberg, et al., “Ion-acoustic solitary waves and spectrally uniform scattering cross section enhancements”, *Ann. Geophys.* 28, 1299–1306, doi:10.5194/angeo-28-1299-2010, 2010.

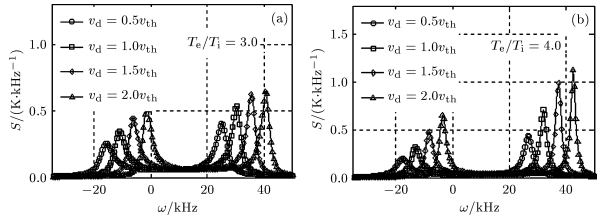


Figure 16: Ion acoustic spectra with different electron-ion temperature ratio and different relative drift of the H^+ and O^+ ions.

Enhanced ion acoustic line in the high ionosphere

The received power of scattered radar signals is sometimes extremely enhanced to up to 2 times above its usual values, and it is mostly contained in the two ion acoustic lines, often asymmetrically. The explanation to this phenomenon has in many publications been proposed to be instability processes. One of these theories includes the ion-ion two-stream instability, which is driven by large relative drifts between two or more ion species, for example a plasma with O^+ with a beam of H^+ . As long as the drift velocity is of the same order of magnitude as the species thermal velocity, the ion acoustic fluctuation level can be enhanced well above the thermal level leading to an enhancement in one or both ion lines. The high relative drift velocity require sufficient acceleration of H^+ which might be possible at high altitudes.

Assuming low energy H^+ ion precipitation and the O^+ ion outflow events, and a H^+ ion distribution function described by a bi-Maxwellian containing the field-aligned heat flow, the enhanced ion acoustic echoes can be interpreted using the ion-ion two-stream instabilities. Then the asymmetry is weakened due to the consideration of field-aligned heat flow.

As shown by Fig. 16, the asymmetry is weaker with increasing electron-ion temperature ratio T_e/T_i . Given a constant electron-ion temperature ratio, however, the incoherent scattering spectrum grows gradually asymmetric when the two-ion relative drift velocity increase.

The change in asymmetry and amplitude of the ion acoustic spectrum with different relative amount of H^+ and O^+ ions is shown in Fig. 17. Although the amplitude of the ion acoustic spectrum is weaker with increasing H^+ content, the corresponding non-asymmetry ratio of the ion acoustic spectrum grows more asymmetric.

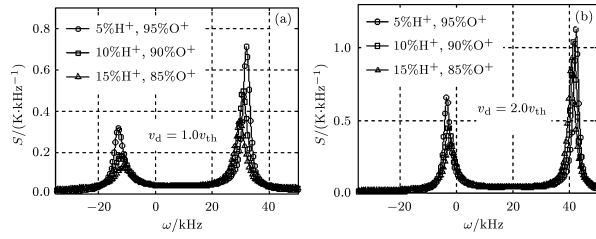


Figure 17: Effects on the ion acoustic spectrum of the relative amounts of H^+ and O^+ ions in the plasma.

X. Kun, et al., "Interpretation on the origin of enhanced ion acoustic line spectra in the high ionosphere", Chin. J. Space Sci. 30, 29–34, (in Chinese) 2010.

Statistical investigation of the Cowling channel efficiency in the auroral zone

The Cowling channel mechanism describes the creation of a secondary polarisation electric field at sharp conductance boundaries in the ionosphere due to excess charges, in the case that the release of these charges to the magnetosphere is fully or partially impeded. The secondary currents generated by the polarisation electric field effectively modify the effective ionospheric conductivity inside the Cowling channel. While the Cowling mechanism is generally accepted for the equatorial electrojet, there is a long-standing discussion about the importance of this mechanism and its efficiency in the auroral electrojet.

A statistical investigation is presented that enables identification of the most probable geospace conditions and MLT locations for a high Cowling efficiency. This investigation is based on more than 1600 meridional profiles of data from the MIRACLE network in Scandinavia, in particular ground magnetic field data from the IMAGE magnetometer network and electric field data from the STARE radar, supported with pointwise ionospheric conductance measurements from the EISCAT radar. The single point conductance measurement that EISCAT provides is crucially important in order to overcome uncertainties caused by unknown boundary values when solving for the electrodynamic parameters along each meridional profile. The data were analysed in the framework of a 3D ionospheric model, but the data set was filtered such that only electrojet-type situations were included, for which the gradients of all measured quantities in longitudinal direction could be neglected. The analysis results in a steep peak of high Cowling channel efficiency probability in

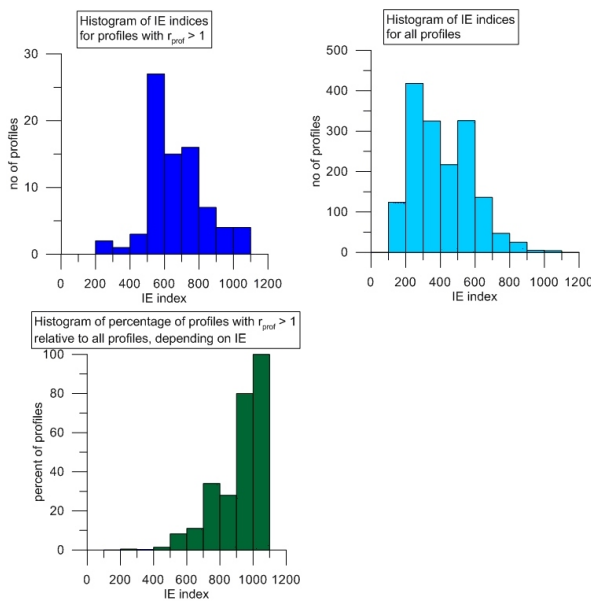


Figure 18: The probability of high Cowling channel efficiency increases almost monotonically with increasing geomagnetic activity.

the early morning sector (0245–0645 MLT), with the largest probability around 05 MLT and for medium and high geomagnetic activity. In agreement with an earlier single event study by Amm and Fujii (2008), this indicates that the Cowling mechanism may be most effective in the early morning part of the central substorm bulge. Further, this analysis results in an almost monotonic increase of the probability of high Cowling channel efficiency with increasing geomagnetic activity (see Fig. 18).

O. Amm, et al., “A statistical investigation of the Cowling channel efficiency in the auroral zone”, *J. Geophys. Res.* 116, A02304, doi:10.1029/2010JA015988, 2011.

Comparison of EISCAT and SuperDARN F-region measurements

Gillies et al. (2010) has compared line-of-sight velocity measurements by SuperDARN with EISCAT tri-static velocity measurements made during the period from 1995 to 1999. It was found that that the velocities measured by SuperDARN were statistically lower than those measured by EISCAT. Part of the discrepancy could be attributed to the fact that the SuperDARN analysis neglects the lower-than-unity refractive index of the scattering structures. The elevation angle measured by SuperDARN was used as a proxy estimate of n_s and this improved the comparison, but the velocities measured by SuperDARN were still consistently

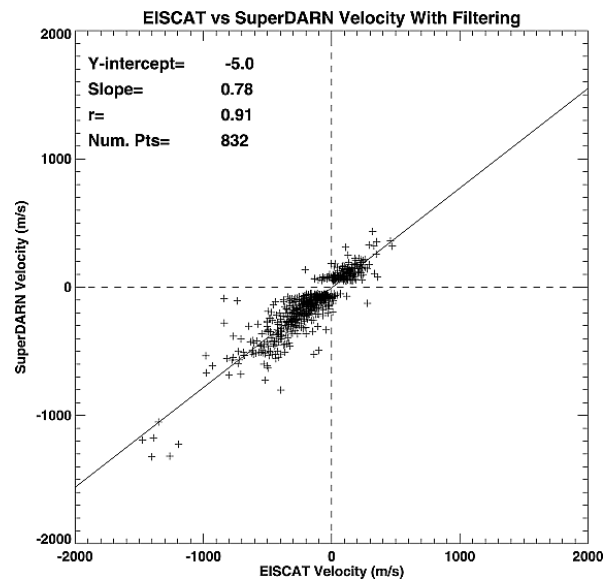


Figure 19: SuperDARN and EISCAT velocity comparison for EISCAT CP-1 and CP-2 modes from 1995 to 1999. SuperDARN points that showed either high standard deviation or little data in the surrounding cells were discarded.

lower. Other estimates of n_s were made using electron densities based on both EISCAT measurements and values from the International Reference Ionosphere model, but these still did not increase the SuperDARN velocities enough to attain the EISCAT values. Gillies et al. (2010) proposed that small-scale dense structures with refractive indices well below unity must exist within the SuperDARN scattering volume and may contribute greatly to the scattering process. These dense, localised structures would provide the density gradients required to generate the coherent irregularities from which the SuperDARN radar waves scatter, whereas EISCAT incoherent radar measurements provide only the background N_e and not the density of the small-scale structures.

R. G. Gillies, et al., “A comparison of EISCAT and SuperDARN F-region measurements with consideration of the refractive index in the scattering volume”, *J. Geophys. Res.* 115, A06319, doi:10.1029/2009JA014694, 2010.

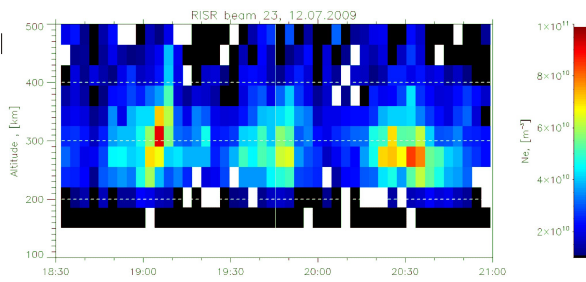


Figure 20: Observation of three polar cap patches as they drift through the most vertical beam of the Resolute Bay AMISR (RISR).

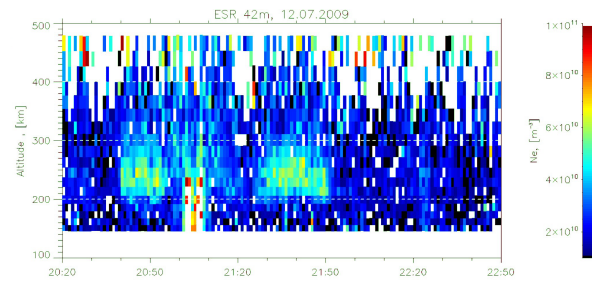


Figure 21: Polar cap patch one and two drifting through the EISCAT Svalbard Radar 42 m beam.

Polar cap studies

Multi-radar study of global polar cap patch dynamics and morphology

In December 2009 a multi radar/optical campaign was performed in order to study the large scale motion of polar cap patches across the polar cap. This was a combined effort by scientists at the University of Tromsø, Boston University, SRI International and the US Air-force Research Laboratory.

Five high latitude incoherent scatter radars were in operation simultaneously (PFISR, RISR, Søndrestrøm, EISCAT UHF and EISCAT Svalbard radar) as well as several all-sky imagers and ionosondes. The geomagnetic conditions during the campaign were quiet and the auroral oval was at times observed to be very small. Polar cap patches were observed on a routine basis throughout the campaign.

In Fig. 20 a series of three patches are observed as they drift through the most vertical beam of the Resolute Bay AMISR (RISR). All three patches could be tracked optically with the all-sky imager located in Qaanaaq as they drifted towards the European sector. Figure 21 shows patch one and two as they drift through the ESR 42 m beam. Patch three missed ESR due to the Earth's rotation and entered the European sector west of Svalbard.

Figure 22 shows the trajectory of patch number one as calculated by the Weimer statistical convection model. It clearly shows how the principal motion across the polar cap of large scale features like polar cap patches can be successfully modelled using statistical models.

M. G. Johnsen, et al., "A multi radar study of global polar cap patch dynamics and morphology", to be submitted, summer 2011.

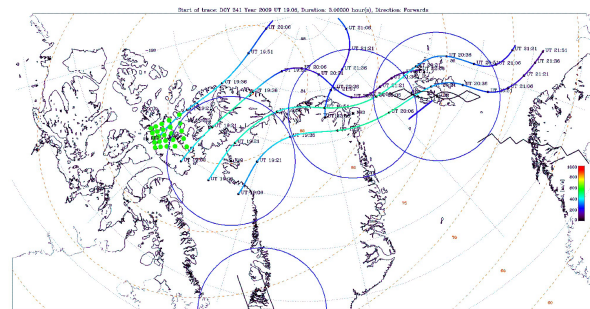


Figure 22: Trajectory of polar cap patch number one calculated by the Weimer statistical convection model.

Seasonal influence on polar cap patches in the high-latitude nightside ionosphere

Three years of ESR data (1999–2001) were used by Wood et al. (2010) to study the influence of seasonality on the patch-to-background density ratio of polar cap patches in the nightside ionosphere observed above northern Scandinavia around solar maximum. Data were selected from periods favourable for patch formation, based on the high-latitude plasma convection pattern, the interplanetary magnetic field, and an absence of in situ precipitation. Patch-to-background ratios of up to 9.4 ± 2.9 were observed between midwinter and equinox, with values of up to 1.9 ± 0.2 in summer. As the patch-to-background ratios in summer were <2 , the enhancements could not formally be called patches; however, they were still significant density enhancements within the anti-sunward cross-polar flow. Aberystwyth University's PLASLIFE (PLASma LIFETIME) computer simulation was used to model the seasonal trend in the patch-to-background ratio and to establish the reasons for the difference between winter and summer values. This difference was primarily attributed to variations in the chemical com-

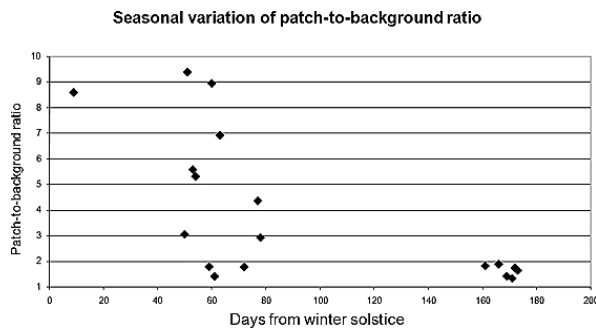


Figure 23: Patch-to-background ratios as a function of the number of days from winter solstice for observations made between 1999 and 2001. When the patch-to-background ratio is <2 , these enhancements are not formally defined as polar cap patches.

position of the atmosphere, which, in summer, both reduced the electron density of the plasma drawn into the polar cap on the dayside and enhanced plasma loss by recombination. A secondary factor was the maintenance of the background polar ionosphere by photo-ionization in summer.

A. G. Wood and S. E. Pryse, "Seasonal influence on polar cap patches in the high-latitude nightside ionosphere", *J. Geophys. Res.* 115, A07311, doi:10.1029/2009JA014985, 2010.

Observations of polar cap patches with the ESR and rockets

There have in recent years been several sounding rocket campaigns at Svalbard. Burchill et al. (2010) used ESR data to study the upflow of thermal ions in the cusp region during the CUSP-2002 sounding rocket flight from Ny-Ålesund on 14 December 2002. They studied the correlation between ion upflow, electron energy fluxes, convection electric fields, VLF/BBELF wave power, and parallel/perpendicular ion temperatures. Lorentzen et al. (2010) used ESR and ground-based optical data to study the formation of a polar cap patch event during the ICI-2 sounding rocket flight from Ny-Ålesund on 5 December 2008, and they developed a conceptual model for how the polar cap patch was created.

Oksavik et al. (2010) used ESR and SuperD-ARN data to study how two intense polar cap patch events on 6 February 2001 drifted across the polar cap from Svalbard to Alaska. Both events had extremely high electron densities (exceeding 10^{12} m^{-3}) when they were first discovered by the ESR in the dayside cusp region over Svalbard, see

Fig. 24. On their way across the polar cap they underwent pulsed flow and substantial rotation. On the nightside the leading edge had become the trailing edge. It suggests that the first patch to enter the dayside polar cap may not always be the first patch to reach the nightside. It also suggests that momentum transfer in the dayside polar cap can last significantly longer than 10 minutes after reconnection, especially for extremely long field lines when IMF B_y is dominating. Knowledge of the solar wind driver and the coupling processes is therefore extremely important for predicting the motion of polar cap patch events across the polar cap. The gradients in the plasma flow associated with the rotation of the extreme density may in itself lead to a stronger growth of ionospheric irregularities that may continue to grow all the way across the polar cap. The result will be more efficient creation of ionospheric irregularities.

J. K. Burchill, et al., "Thermal ion upflow in the cusp ionosphere and its dependence on soft electron energy flux", *J. Geophys. Res.* 115, A05206, doi:10.1029/2009JA015006, 2010.

D. A. Lorentzen, et al., "In situ measurements of a newly created polar cap patch", *J. Geophys. Res.* 115, A12323, doi:10.1029/2010JA015710, 2010.

K. Oksavik, et al., "On the entry and transit of high-density plasma across the polar cap", *J. Geophys. Res.* 115, A12308, doi:10.1029/2010JA015817, 2010.

The open-closed field line boundary

In a study by Woodfield et al. (2010) previous work was revisited which used two EISCAT radars to track the motion of the Open-Closed field line Boundary (OCB). The location of the OCB enables the size of the polar cap to be established, which is very important for understanding substorm processes and reconnection rates in general. In previous studies, one radar was used to observe the latitudinal variation of F-region electron temperature, while the second one was used to estimate the background variation of T_e with altitude which was then subtracted from the measurements in the first radar beam in order to identify the electron temperature enhancement corresponding to the OCB. Woodfield et al. demonstrated that the use of a model such as the International Reference Ionosphere 2007 (IRI-2007) can remove the requirement for the second radar and therefore increase the number of cases in which the background T_e subtraction can be performed. Applying the modified technique to some substorm

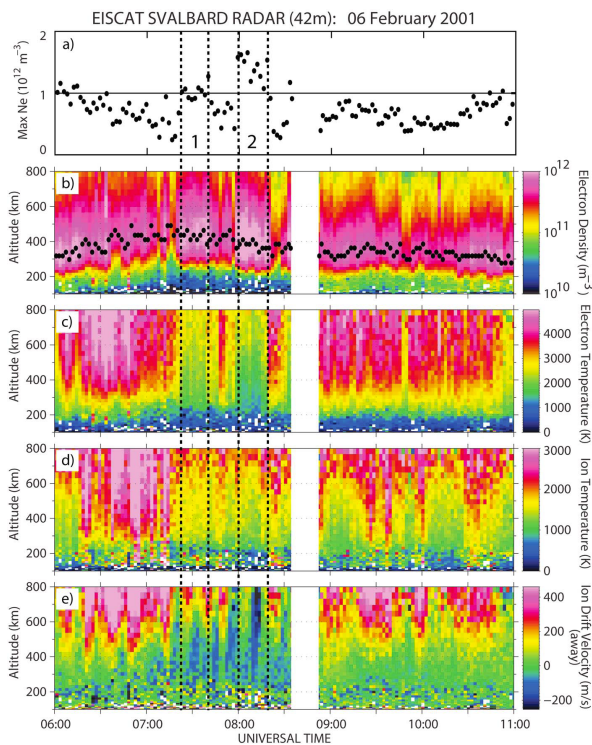


Figure 24: ESR and SuperDARN data of two intense polar cap patch events on 6 February 2001 drifting across the polar cap from Svalbard to Alaska.

intervals, it was found that the IRI-2007 method produces an OCB proxy location which on average is 0.25° degrees equatorward (in AAGCM coordinates) of the boundary location produced by the two-radar method. Comparing both methods with OCB locations inferred from DMSP particle data and IMAGE satellite data, they found that both methods performed quite well, and neither method was particularly favoured over the other. The magnitude of the mean offset to the IMAGE OCB was found to vary between 0.1° and 2.7° in latitude, depending on the event and the IMAGE camera used.

E. E. Woodfield, et al., "Combining incoherent scatter radar data and IRI-2007 to monitor the open-closed field line boundary during substorms", *J. Geophys. Res.* 115, A00I15, doi:10.1029/2010JA015751

Polar cap boundary location using IMAGE and EISCAT

The ionospheric Polar Cap Boundary (PCB) can be determined using different methods. In a study of Hubert et al. (2010), electron temperatures from

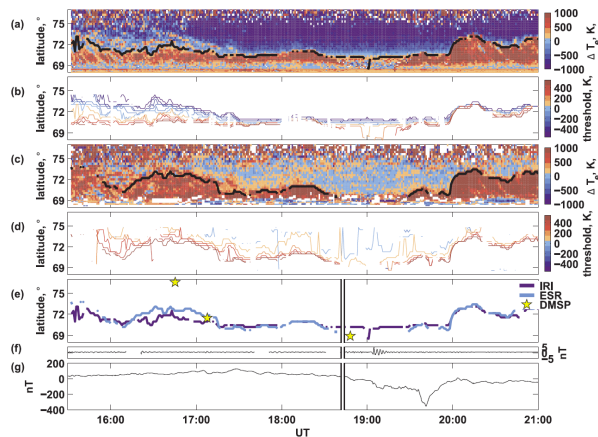


Figure 25: The data are from 29 October 2004. (a and c) ΔT_e with overlaid bT_e (black line) from the IRI ($T_{et} = 100$ K) and ESR ($T_{et} = 500$ K) methods, respectively; (b and d) the full range of boundaries from T_{et} ranging from -500 to 500 K for the IRI and ESR methods, respectively; (e) bT_e from the IRI and ESR methods (vertical white on black line is substorm onset time from the Frey et al. (2004) list, and yellow stars indicate DMSP b6 identifications); (f) Pi2 filtered (20–200 s) H component magnetometer data from Lerwick, United Kingdom; (g) H component magnetometer data from Kilpisjärvi, Finland.

observations of the EISCAT radar facility were used to estimate the latitude of the PCB along the meridian of the EISCAT VHF beam. The second method for estimating PCB utilised global images of proton aurora obtained by the FUV SI12 instrument of the IMAGE satellite. In two events, the agreement between the two methods was good and the mean of the difference was within the resolution of the observations (see Fig. 26). In a third event, the PCB estimated from EISCAT data was located several degrees poleward of that obtained from the IMAGE FUV SI12 instrument, suggesting electron precipitation poleward of the proton aurora. In addition, a search for the location of the east-west equivalent current reversal, known as the Magnetic Convection Reversal Boundary (MCRB), was made. The MCRB from the MIRACLE magnetometer chain followed mainly the motion of the polar cap boundary during different substorm phases, but differences arose near the Harang discontinuity.

O. Hubert, et al., "Comparison of the open-closed field line boundary location inferred using IMAGE-FUV SI12 images and EISCAT radar observations", *Ann. Geophys.* 28, 883–892, 2010.

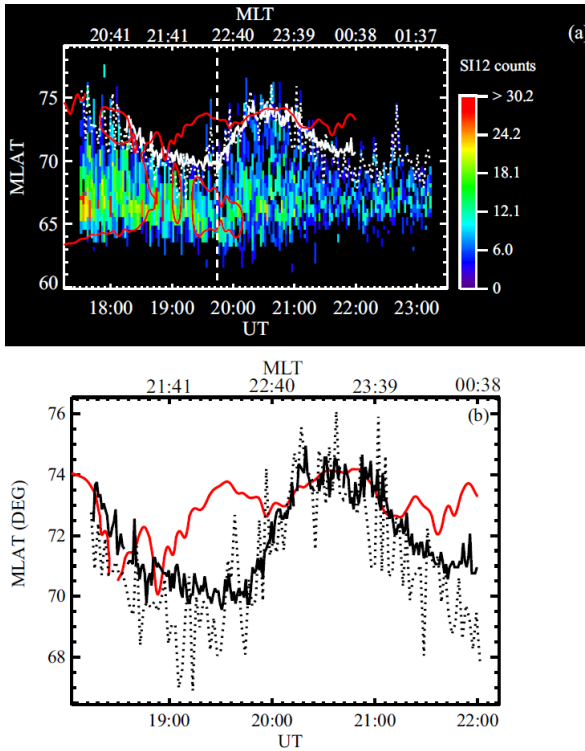


Figure 26: (a) Keogram of SI12 counts along the meridian corresponding to the EISCAT field of view on 22 September 2001. The overlaid white solid line represents the location of the EISCAT PCB, the dotted lines show the SI12 PCB, and the red solid lines represent the MCRBs as determined using the MIRACLE magnetometer data. The vertical dashed line indicates the beginning of net flux closure. (b) Blowup of the polar cap boundaries determined during the interval with simultaneous EISCAT observations, with the same line conventions as in panel (a).

Polar cap signatures

Detection of the Polar Cap Boundary (PCB) was made by German EISCAT users in collaboration with colleagues from Finland. Within the F region polar cap the electron temperature is reduced compared to the surrounding auroral oval and this change can be utilised to determine the polar cap boundary. This method was tested by EISCAT and coinciding satellite observations by CHAMP. The increase in the electron temperature within in the auroral oval is generated by the collisional heating of the background plasma due to primary and secondary electrons (Aikio et al. 2006). For polar cap identification, the variations of small-scale Field-Aligned Currents (FAC) and electron temperatures as observed by CHAMP on polar passes were used (Ritter et al. 2010). The PCB can be de-

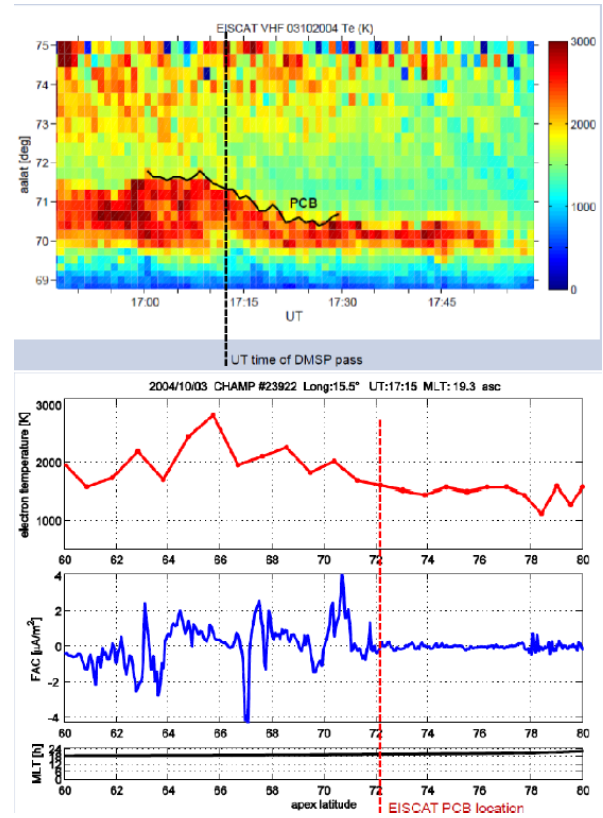


Figure 27: Polar cap boundary detection using the electron temperature as measured by EISCAT VHF radar (top panel) and the CHAMP data of the electron temperature and the field-aligned current density (bottom panels). The vertical lines indicate the overpass of CHAMP and the EISCAT PCB location.

tected clearly by a sudden drop of FAC density. The found PCB latitude coincides very well with the sharp electron temperature decrease that can be observed by the EISCAT VHF radar, as shown in Fig. 27.

A. Aikio, et al., "Method to locate the polar cap boundary in the nightside ionosphere and application to a sub-storm event", *Ann. Geophys.* 24, 1905–1917, 2006.

P. Ritter, et al., "Signature of the polar cap in ionospheric currents and electron temperature as observed by CHAMP", Poster at AGU 2010 Fall Meeting, San Francisco, US, Dec. 13–17, 2010.

P. Ritter, et al., "Signature of the polar cap in ionospheric currents and electron temperature as observed by CHAMP", Poster at AEF Spring Meeting, Köln, Germany, Feb. 21–24, 2011.

Studies of particle precipitation and the aurora

Determination of the characteristic energy of precipitating electrons

Energetic electrons (tens to hundreds of keV) deposit significant amounts of energy into the D layer of the ionosphere. Riometers provide a means of monitoring this electron precipitation by measuring the associated Cosmic Noise Absorption (CNA), but individually they are incapable of resolving the associated energy. However, the combination of two imaging riometers with overlapping beams allows an estimate of the height of peak CNA, and hence the associated energy, to be made. Wild et al. (2010) examined two methods for estimating the height of CNA, using data from two imaging riometers in northern Fennoscandia; a 3-D reconstruction of CNA using Occam's inversion and a technique based upon the triangulation of discrete absorption structures were developed. The results of these methods were then compared with results from a previously published technique. It was found that, for these case studies, the height triangulation and 3-D reconstruction offered improvement over previous methods. These techniques were tested using data from the EISCAT VHF radar. The observations showed a good correlation between the estimates of peak height of CNA from EISCAT and from the triangulation and 3-D reconstruction methods. Three case studies were examined in detail — a slowly varying absorption event, an afternoon spike, and an evening absorption spike event — and estimates of the characteristic energy of the precipitating particles were made. The substorm event had a characteristic energy of ~ 5 keV, whereas the characteristic energy for the morning event was 17–20 keV. The analyses indicated that the afternoon spike event was the most energetic, having a characteristic energy greater than 100 keV.

P. Wild, et al., "Triangulating the height of cosmic noise absorption: A method for estimating the characteristic energy of precipitating electrons", *J. Geophys. Res.* 115, A12326, doi:10.1029/2010JA015766, 2010.

Acceleration mechanism for flickering aurora

An analysis has been presented by Whiter et al. (2010) of flickering (2–10 Hz) auroras observed with a state-of-the-art multispectral imaging sys-

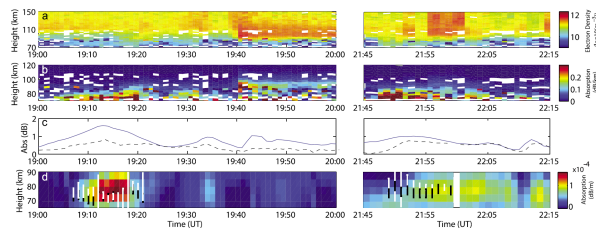


Figure 28: From top to bottom: (a) EISCAT Electron density. ($\log_{10}(\text{m}^{-3})$). (b) Absorption profile using EISCAT electron density (dB/km). (c) Absorption in beam 9 of IRIS (solid line) and beam 656 of ARIES (dashed line) (dB). These beams intersect at 71 km. (d) Vertical absorption profiles using the tomographic method (69.5° latitude, 19.2° longitude) with the peak height of CNA marked on in black from EISCAT. Error bars generated using the length of the range gate. Height triangulation method is marked in white (only cross-correlation values over 0.6), 22 May 2008, 19:00–22:30 UT. Data between 20:00 UT and 21:45 UT are not shown as there was no activity.

tem, Auroral Structure and Kinetics (ASK), located at the EISCAT site in Tromsø. Short (1–2 s) periods of flickering aurora were identified in which the frequency of the brightness oscillations decreased or increased smoothly over time. This study is believed to be the first detailed analysis of such "chirps", or field-aligned bursts, in flickering aurora. The authors found that the electron precipitation energy was strongly anti-correlated with the flickering frequency during all the identified chirps. This result is consistent with the theory that flickering aurora is caused by the resonance interaction between electromagnetic ion cyclotron waves and precipitating electrons and that the wave parallel phase velocity is the primary factor determining the electron acceleration produced by this mechanism. The authors concluded that no other current theories could completely explain these observations.

D. K. Whiter, et al., "Using multispectral optical observations to identify the acceleration mechanism responsible for flickering aurora", *J. Geophys. Res.* 115, A12315, doi:10.1029/2010JA015805, 2010.

Studies of dust and meteorites

ECOMA sounding rocket campaign

In 2010 extensive EISCAT measurements were performed by German scientists and connected to the ECOMA-2010 sounding rocket campaign. The

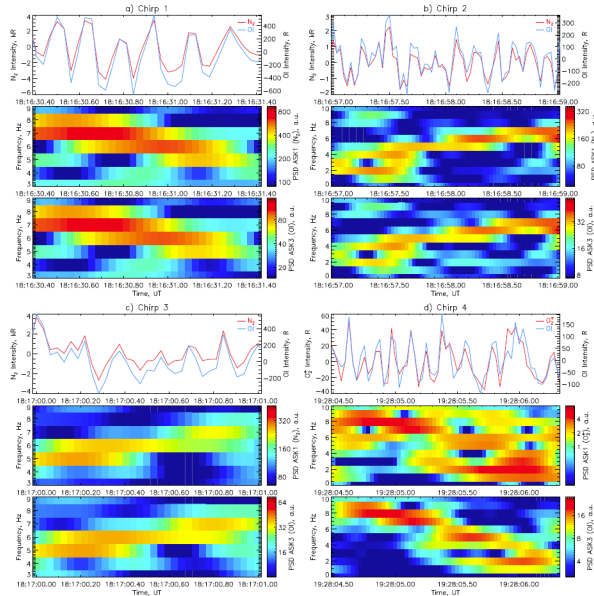


Figure 29: For each chirp, the first panels show the detrended intensity time series from the ASK1 (N_2 or O_2^+) and ASK3 (OI) cameras. The second and third panels show the power spectra obtained from these time series for ASK1 and ASK3 respectively.

ECOMA (Existence and Charge state Of Meteoric smoke particles in the middle Atmosphere) campaign was conducted at Andenes (Andøya Island, Norway, $69^\circ N$, $16^\circ E$) in December 2010. During this period a strong meteor shower, the Geminides, was approaching the Earth's orbit and many meteors were even visually observed. Three instrumented rockets were launched to investigate meteoric smoke particles. The principle of the new rocket-borne ECOMA particle detector, which is a combination between a classical Faraday cup and Xenon flashlamps for active photoionization of meteoric dust particles and their subsequent detection of corresponding photoelectrons, was introduced by Rapp and Strelnikova (2009). Detailed results of previous rocket launches were already published by Rapp et al. (2010) which clearly describes the instrumentation of the rocket payload and the scientific results.

The ECOMA campaign was supported by several ground based instruments (mainly radars and lidars) near the rocket launch area as well as by the EISCAT VHF radar. In summary, more than 80 hours of EISCAT radar observations were realised in the early morning hours, where the highest number of meteors is detected. The backscattered echoes from the EISCAT radar were analysed to determine the spectral properties of these echoes.

This analysis is based on the detailed investigation of the spectral shape and the shape of the Auto-Correlation Function (ACF) as described by Rapp et al. (2007) and Strelnikova and Rapp (2010).

Some initial results of the EISCAT VHF radar data are shown in Fig. 30. The plot shows the estimated electron densities for the measurements. Analysing the corresponding ACFs averaged over the whole period with respect to the spectral shape, the n parameter is less than 1 at altitudes between 75 and 80 km, the altitude range where meteor dust particles are expected. According to the analysis by Strelnikova and Rapp (2010) the fitting parameter $n < 1$ indicates the presence of charged particles, in this case meteoric smoke particles. Importantly, these preliminary n values are in good agreement with initial results obtained with the particle detector on the ECOMA rockets.

M. Rapp, I. Strelnikova, and J. Gumbel (2007), "Meteoric smoke particles: Evidence from rocket and radar technique", *Adv. Space Res.* 40, 809–817, doi:10.1016/j.asr.2006.11.021, 2007.

M. Rapp, and I. Strelnikova, "Measurements of meteor smoke particles during the ECOMA-2006 campaign: 1. Particle detection by active photoionization", *J. Atmos. Solar-Terr. Phys.* 71, 477–485, doi:10.1016/j.jastp.2008.07.011, 2010.

M. Rapp, et al., "Rocket-borne in situ measurements of meteor smoke: Charging properties and implications for seasonal variations", *J. Geophys. Res.* 115, D00I16, doi:10.1029/2009JD012725, 2010.

I. Strelnikova, and M. Rapp, "Studies of polar mesosphere summer echoes with the EISCAT VHF and UHF radars: Information contained in the spectral shape", *Adv. Space Res.* 45, 247–259, doi:10.1016/j.asr.2009.09.007, 2010.

Solar wind studies

Interplanetary scintillation observations

A number of papers focusing on the use of EISCAT interplanetary scintillations (IPS) data appeared in a special issue of *Solar Physics*, resulting from a workshop on the remote sensing of the inner heliosphere, held in Aberystwyth in 2009.

Bisi et al. (2010a) summarised results from ten years of EISCAT observations of Stream Interaction Regions (SIRs) in the solar wind (1994 to 2003). Previous studies had shown that SIRs were characterized by intermediate-velocity solar

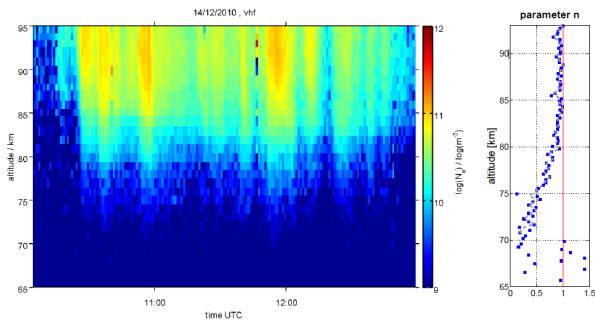


Figure 30: Raw electron density observed on Dec. 14th, 2010, with the EISCAT VHF radar (left). From the analysis of the shape of the ACFs the averaged fitting parameter n for the observational period is determined (right). (Courtesy of G. Teiser, 2011.)

wind and, in the case of compressive interactions, higher levels of scintillation. Bisi et al. found that, after dismissing intermediate-velocity observations associated with solar-wind transients (such as coronal mass ejections) the remaining intermediate velocities lay above coronal structures where stream interaction would be expected. The early stages of developing compression regions, on the leading edges of compressive stream interaction regions, were clearly detected as close to the Sun as $30 R_{\odot}$. The same approach was applied to study non-compressive interaction regions (shear layers) between solar-wind streams of different velocities, where the stream interface lay at near-constant latitude. The results confirmed that intermediate velocities seen in IPS observations above stream boundaries may arise from either compression regions, or from non-compressive shear layers. The variation in velocity was comparable in compressive and non-compressive regions — a result which may contain important information on the geometry of developing SIRs. It is clear from these results that compressive and non-compressive interaction regions belong to the same class of stream-stream interaction, with the dominant mode determined by the latitudinal gradient of the stream interface.

Bisi et al. (2010b) reported results from a multi-instrument coordinated study of the solar eruptive event of 13 May 2005, discussing the resultant Earth-directed (halo) Coronal Mass Ejection (CME), and its effects on the terrestrial space environment and upper atmosphere. The Interplanetary CME (ICME) impacted the Earth's magnetosphere and caused the most intense geomagnetic storm of 2005, with a Disturbed Storm Time (Dst) index reaching -263 nT at its peak. The terrestrial

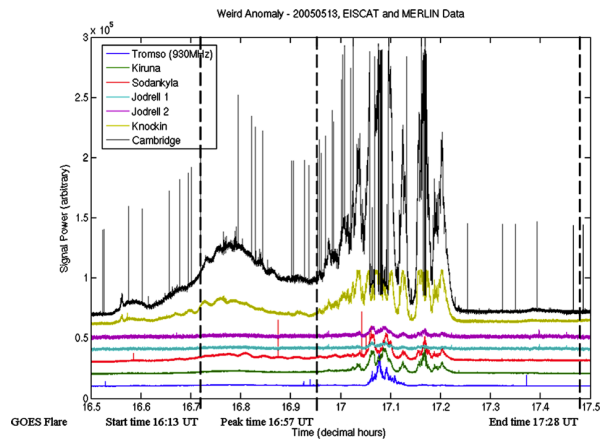


Figure 31: Observations of radio signals from EISCAT and MERLIN showing the anomalous signal-strength enhancement on 13 May 2005 due to the flare/CME and associated coronal radio burst overwhelming the IPS signal as taken from Jones et al. (2006). All EISCAT and MERLIN observations were made at 1420 MHz with the exception of one (as marked in the figure).

environment responded to the storm on a global scale. Combined observations from coronal and interplanetary remote-sensing instruments, interplanetary and near-Earth in-situ measurements, remote-sensing observations and in-situ measurements of the terrestrial magnetosphere and ionosphere, along with coronal and heliospheric modelling, were used to trace the origin, development, propagation, terrestrial impact, and subsequent consequences of this event, to obtain the most comprehensive view of a geo-effective solar eruption to date.

Bisi et al. (2010c) examined EISCAT data obtained during the April/May 2007 observing campaign to study the solar wind velocity structure during the declining phase of Solar Cycle 23. Many co-rotating and transient features were observed during this period. Tomographic reconstruction analysis was used to map the velocity structure of the inner heliosphere and the results compared to a number of optical and other measurements made by spacecraft during this interval. The reconstructions showed clear co-rotating regions during this period, and the time-series extraction at spacecraft locations compared well with measurements made by the STEREO, Wind, and ACE spacecraft. This was the first time that such clear structures have been revealed using this 3D technique with EISCAT IPS data as input.

Dorrian et al. (2010) discussed the detection and evolution of a complex series of solar-wind struc-

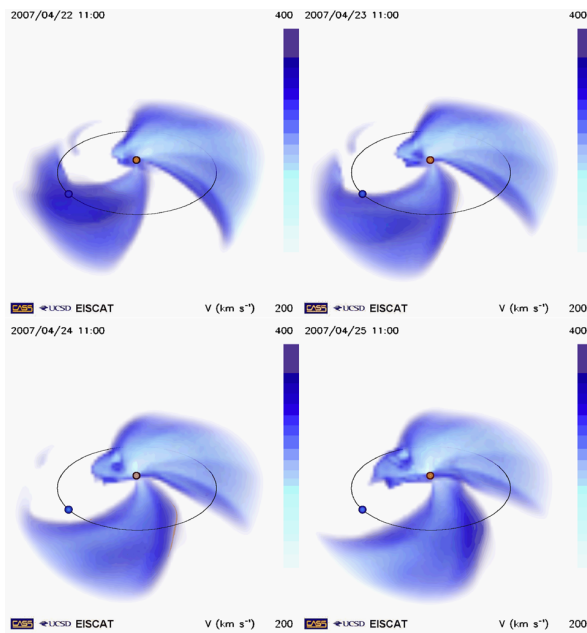


Figure 32: A set of four velocity 3D views showing the slow-wind portions of co-rotating structures at the dates and times shown (the higher-velocity portions are not shown for clarity of viewing). These images form part of a movie (available online) covering this entire period. The Earth is shown as a blue sphere towards the bottom-left of each image along with its orbital path shown in black. The orange/red sphere in the centre of each image represents the Sun (neither the Earth or the Sun spheres are to scale).

tures in the days following the comet 2P/Encke tail disconnection event in April 2007. EISCAT data were used to characterise the evolution of transient solar-wind structures ranging in size from $<10^5$ km to $>10^6$ km, and data from STEREO were used to place them in context. One transient in the slow wind was observed being swept up and entrained by an SIR, which was later detected in-situ at Venus by the ASPERA-4 instrument on VEX. This observation provides the first indication of heliocentric distances at which such transients can become entrained. Dorrian et al. suggested that the solar-wind transients may be the interplanetary counterparts of structures reported from coronagraph observations and the transient magnetic structures reported from in-situ measurements in interplanetary space.

Whitaker et al. (2010) reported the first combination of IPS data with in-situ plasma measurements from Venus Express. The ion mass analyser instrument on VEX was used to investigate solar wind interaction with the Venusian magneto-

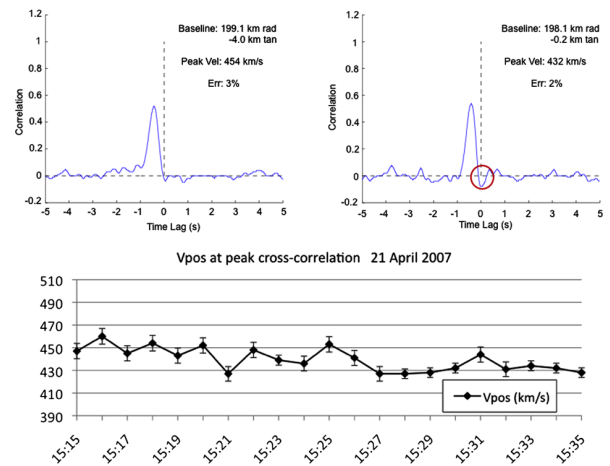


Figure 33: Sample cross-correlation functions (top left and right panels) from observations of IPS on 21 April 2007, one showing the appearance of anticorrelation (circled) near zero time lag, indicating the presence of magnetic field rotation in the ray path. Each cross-correlation function is produced from a ten-minute data bin. Field rotations are observed on timescales as short as 15 minutes, suggesting structures with scale sizes of less than 400,000 km, placing them in the small-scale transient category. The bottom plot shows the variation in V_{pos} recorded over the course of the observing run (times indicate the start of each ten-minute bin).

sphere in the presence of two different solar wind phenomena; a CIR and a CME. The CIR, detected with IPS and sampled in-situ at Venus, was found to dramatically affect upstream solar wind conditions.

Jackson et al. (2010) reported the extension of the UCSD three-dimensional tomographic technique for solar wind imaging, which already uses input data from a range of in-situ and ground-based instruments, including EISCAT. Their study examined the use of in-situ spacecraft data for constraining the time-dependent tomographic solutions. Jackson et al. demonstrated that, although the largest effect on the reconstructions is seen close to the locations of the in-situ constraining measurements, their inclusion significantly reduces the error of the global 3D reconstruction. The effect is to improve the real-time measuring technique, as well as to enable more accurate forecasting.

M. M. Bisi, et al., "Interplanetary Scintillation Observations of Stream Interaction Regions in the Solar Wind", *Solar Physics* 261(1), 149–172, DOI: 10.1007/s11207-009-9471-1, 2010a.

M. M. Bisi, et al., "From the Sun to the Earth: the 13 May 2005 Coronal Mass Ejection", *Solar Physics* 265(1-2), 49–127, DOI: 10.1007/s11207-010-9602-8, 2010b.

M. M. Bisi, et al., "Three-Dimensional (3-D) Reconstructions of EISCAT IPS Velocity Data in the Declining Phase of Solar Cycle 23", *Solar Physics* 265(1-2), 233–244, DOI: 10.1007/s11207-010-9594-4, 2010c.

G. D. Dorrian, et al., "Transient structures and stream interaction regions in the solar wind: Results from EISCAT interplanetary scintillation, STEREO HI and Venus Express ASPERA-4 observations", *Solar Physics* 265(1-2), 207–231, DOI: 10.1007/s11207-010-9599-z, 2010.

B. V. Jackson, et al., "Inclusion of in-situ measurements into the UCSD time-dependent tomography to constrain and better forecast remote-sensing observations", *Solar Physics* 265, 245–256, 2010.

I. C. Whitaker, et al., "In-situ observations of a co-rotating interaction region at Venus identified by IPS and STEREO", *Solar Physics* 265, 197–206, 2010.

Studies of fundamental plasma physics

Ray tracing analysis of L mode pumping of the ionosphere

The "magnetic zenith effect" had first been observed with the Heater several years ago as an increased plasma response to Ordinary (O) mode pump waves and optical emissions around the Magnetic Zenith (MZ). Using ray tracing of ordinary mode HF waves in an ionosphere with kilometre-scale field aligned density depletions, or ducts, Nordblad and Leyser (2010) have now found that transmission across the plasma resonance becomes possible at new locations as rays are guided into the so-called L mode (Fig. 34). Stronger transmitted fields are seen in some directions, notably at inclinations close to the vertical or the MZ. It is argued that the results could have implications for the MZ.

E. Nordblad, and T. B. Leyser, "Ray tracing analysis of L mode pumping of the ionosphere, with implications for the magnetic zenith effect", *Ann. Geophys.* 28, 1749–1759, doi:10.5194/angeo-28-1749-2010, 2010.

Observations of heating experiments in the low ionosphere in polar winter

Based on super-Gaussian incoherent scatter theoretical model, the LM (Levenberg-Marquart) arith-

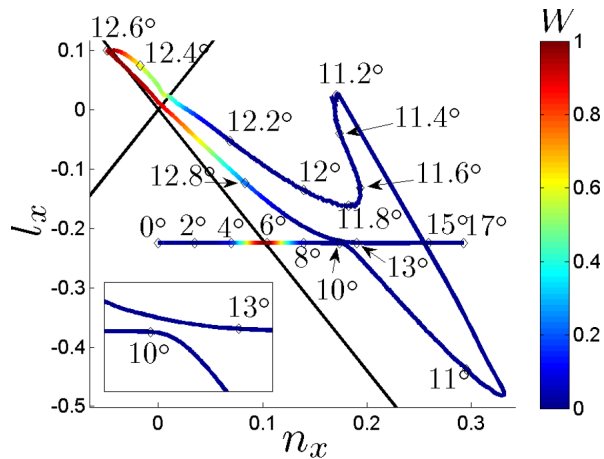


Figure 34: The critical index of refraction, n_x and the parameter l_x , are plotted for a succession of rays in the meridional plane. The values of n_x and l_x are taken at the point of closest approach to the plasma resonance. The ionosphere has a 3% density reduction close to the magnetic zenith. The long black line represents the radio window at $n_x = -l_x \sqrt{Y/(1+Y)}$. The colour indicates the transmission factor, which reaches 1 at the radio window. The curve returns to the black line in the upper left corner of the figure, as rays propagating in the duct reach the radio window and are transmitted.

metic has been used to fit the incoherent scatter spectra at 100 km altitude measured by EISCAT UHF during the ionospheric heating campaign operated in X-mode at 10:08, 10:16, 10:24, 10:40, 10:56 UT and in O-mode at 10:32 and 10:48 UT on January 11th, 2008. The measured incoherent scatter spectra of these seven heating cases and a comparison between fitting results of GUIDAP and the super-Gaussian model is shown in Fig. 35. GUIDAP uses two assumptions, that is that the ionosphere plasma is in equilibrium and that the electron and ion temperature ratio is constant. This may bring some errors when fitting results. Particularly, when the pumping is in X-mode, the fitting results of GUIDAP will be much higher than the measured ones. By using the super-Gaussian model with the introduction of independent electron temperature and non-Maxwellian index, however, a better fitting result can be achieved. Furthermore, the peak power in O-mode at 10:32 and 10:48 UT respectively is obviously higher than that of the four X-mode heating at 10:08, 10:24, 10:40 and 10:56 UT.

X. Bin, et al., "Observations of the heating experiments in the polar winter ionosphere — Analysis in low re-

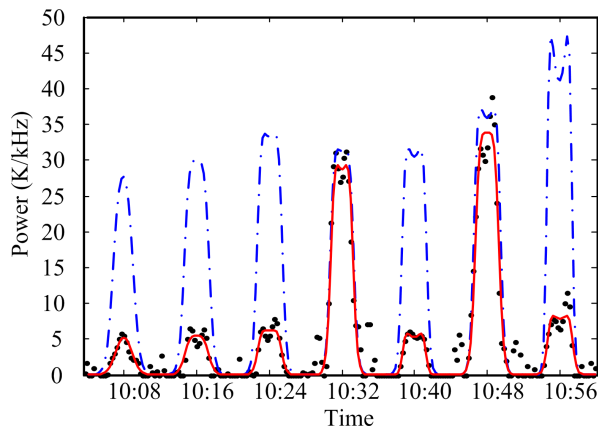


Figure 35: The measured and fitted power spectral densities of the seven heating cases (dots: measured data; dash-dotted line: fit results of GUISDAP; solid line: fit results of the super-Gaussian model).

gion", Chinese Journal Geophysics 53, 1263–1268, (in Chinese) 2010.

Activities by the Arctic and Antarctic Research Institute (AARI) in 2010

Two extensive HF heating campaigns were held by the Arctic and Antarctic Research Institute (AARI), Russia, in March and November 2010 in a close collaboration with the Leicester University (Prof. T. Yeoman) related to studies of small-scale artificial field-aligned irregularities (AFAIs) in the F-region of the ionosphere under X-mode heating. It is well known that AFAIs occur at the upper hybrid resonance altitude due to the thermal parametric (resonance) instability when ordinary (O-mode) polarised HF pump waves reach the ionospheric reflection height. Since the resonance altitude in the ionosphere cannot be reached by an extraordinary polarisation (X-mode) HF pump wave, only O-mode waves can excite AFAIs. The results obtained clearly demonstrate that the X-mode HF pump wave, radiated into the magnetic zenith from the EISCAT/Heating facility, can also generate very strong AFAIs in the high-latitude F-region ionosphere when the heater frequency is above f_{oF2} but comparable to the extraordinary mode critical frequency, $f_{xF2} \approx f_H > f_{oF2}$.

The experiments were carried out on 5, 6 and 8 March 2010 and on 4, 5, 6, 7 and 10 November 2010. The EISCAT HF heating facility (69.6°N, 19.2°E; magnetic dip angle $I = 78^\circ$) was used to modify the ionosphere in the high-latitude F region. The HF heater antenna beam was tilted 12°

to the south of zenith, thus allowing HF pumping in the field-aligned direction (magnetic zenith, MZ). In the course of the experiments the heating facility was operating at 3.95, 4.04, 4.9128, and 5.423 MHz, with X-mode polarization, and with 10 min continuous HF pulses. The experiments were carried out during quiet magnetic conditions.

The modified ionospheric F region was probed by the CUTLASS Hankasalmi, Finland radar (63°N, 27°E). The CUTLASS (Finland) radar transmitter site is located approximately 1000 km south of the Tromsø heating facility. In the course of experiments the CUTLASS radar was running a non-standard mode optimised for observation of heating effects over Tromsø with one fixed beam (beam 5) with a high temporal and spatial resolution. It operated almost simultaneously at several frequencies from ~10 to 17 MHz and was therefore sensitive to AFAIs with the spatial size across the geomagnetic field of the order of $l_\perp \approx 15 - -9$ m respectively. The HF heating facility at Tromsø is located adjacent to the EISCAT UHF incoherent radar (930 MHz). During the experiments the UHF radar measured the ionospheric plasma parameters in the direction of the magnetic zenith. Ionograms, taken every four minutes using the EISCAT ionosonde (dynasonde), indicated a smooth F2 layer with the critical frequency f_{oF2} below the heater frequency, f_H , by 0.4–0.6 MHz. At the same time the heater frequency was near or just below the extraordinary mode critical frequency (f_{xF2}). Therefore, it was suggested that the HF pump wave with X-mode polarisation was reflected from the ionosphere. Figure 36 shows the CUTLASS Hankasalmi backscatter power during the experiment on 6 March 2010.

Before the X-mode heating, the HF pump wave with O-mode polarisation was radiated for the first two heater-on periods. It is seen from Figure 36 that the intense signals scattered from AFAIs, excited by the HF pump wave with O-mode polarisation, were observed at three CUTLASS frequencies in the heater-on period from 15:26–15:36 UT, when the electron density in the F region dropped, and the heater frequency, $f_H = 4.9128$ MHz, was near and then slightly above the critical frequency of F2 layer, $f_{oF2} = 4.7 - -4.9$ MHz. During the heater-on period from 15:41–15:51 UT the values of f_{oF2} became ~4.4 MHz and the signals scattered from AFAIs disappeared at 17 MHz. At 10 and 13 MHz the weak scattered signals were observed during the first 3–4 minutes of the 10 min heating cycle and

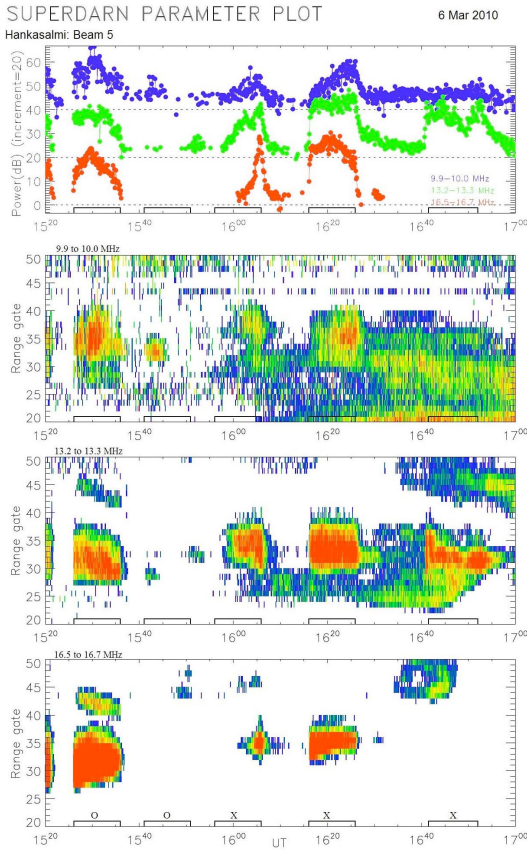


Figure 36: Backscattered power from the Hankasalmi (Finland) CUTLASS radar (beam 5) at operational frequencies of about 10, 13 and 17 MHz for contrasting O/X-mode heating on 6 March 2010 between 15:20 and 17:00 UT. The behaviour of the backscattered power at every operational frequency averaged over three 15 km gates, corresponding to the central part of the heated beam is shown in the top panel and their behaviour in the range-gate – universal time UT coordinates are given in the bottom panels. O/X-mode heater-on periods are marked in the time axis.

then disappeared. The polarisation of the HF pump wave was changed from O to X-mode in the next heater-on period from 15.56–16.06 UT. The polarisation change of the heater wave produced scattered signals over Tromsø at three CUTLASS frequencies. On 6 March 2010, X-mode heating was performed during three consecutive heating cycles. The distinctive features of X-mode AFAIs with different spatial size across the geomagnetic field are clearly seen from the behaviour of the backscattered power at every operational frequency averaged over three 15 km gates, corresponding to the central part of the heated beam (see the top panel in Figure 36). The excitation of AFAIs

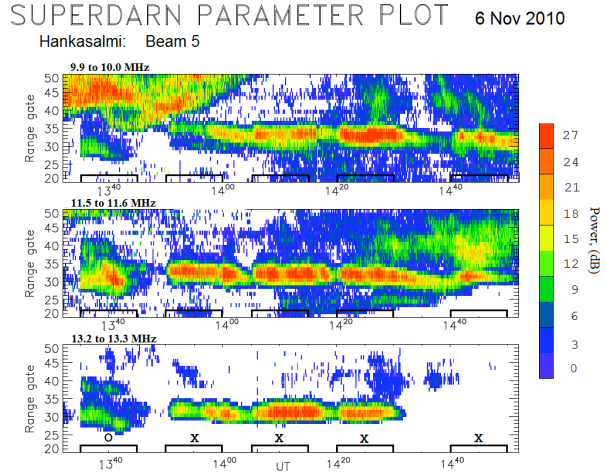


Figure 37: Backscattered power from the Hankasalmi (Finland) CUTLASS radar (beam 5) at operational frequencies of about 10, 11.5 and 13 MHz in the range-gate – universal time UT coordinates for contrasting O/X-mode heating on 6 November 2010 between 13:30 and 15:00 UT. O/X-mode heater-on periods are marked in the time axis.

with $l_{\perp} \approx 11$ m, responsible for the CUTLASS backscatter, occurred in all three heater-on periods. They appeared within a time interval from 10 s to 3 minutes after the heater was turned on. Their decay time was approximately 6 and 15 min after the first and second X-mode cycle respectively.

The results of the experimental observations on 5 March 2010 are very similar to the case of 6 March 2010 but in this experiment only AFAIs with $l_{\perp} \approx 15$, 11, and 9 m were excited. In the course of the experiment on 8 March 2010 the HF pump wave was radiated at frequency of $f_H = 5.423$ MHz. It was the only experiment when O-mode heating at the same frequency was not carried out prior to the X-mode heating. Nonetheless during the experiment on 8 March 2010 the AFAIs with different spatial sizes of $l_{\perp} \approx 15$, 11 and 9 m were excited in four consecutive 10 min heater-on periods.

A very similar behaviour of AFAIs in the F region of the ionosphere excited by HF pump wave with X-mode of polarisation was observed during experiments on November 2010. Figure 37 shows the CUTLASS Hankasalmi backscatter power during the experiment on 6 November 2010.

EISCAT UHF incoherent scatter data from Tromsø site, obtained in the direction of the magnetic zenith, were examined to estimate the changes in the electron temperature (T_e) and electron density (N_e) at different altitudes, accompa-

nying the generation of AFAIs induced by the powerful HF radio waves with X-mode polarization. The results obtained for contrasting O/X-mode heating clearly demonstrate that an HF pump wave with X-mode polarization heats the ionosphere through collision processes more effectively than an O-mode HF heater wave. This is in agreement with the recent results of Gustavsson et al. (2010) who showed that heating of ionospheric electrons is more efficient for X-mode heating than for O-mode heating. In our experiments the T_e enhancements under X-mode heating reached values of $\sim 50\%$, above the background level over an altitude range from 186 to 247 km.

Temporal variations of T_e with 30 s integration time at different altitudes in the direction of the magnetic zenith during the experiment on 6 March 2010 are plotted in Fig. 38. As was also shown in Fig. 36, weak scattered signals were observed at 10 and 13 MHz during the O-mode heating cycle from 15:41–15:51 UT. Therefore not only the pure ohmic heating was observed here. During the next three consecutive X-mode heating cycles T_e enhancements of up to 50% above the background level occurred. The strongest T_e enhancements took place at 214 km from 16:16–16:26 UT cycle. The electron density behaviour in the magnetic zenith (Fig. 39) shows some interesting features. It is seen that N_e increased by up to 30% above the background level at an altitude of 282 km during the X-mode heating cycles. N_e enhancements were also observed at 246 km, however no significant enhancements were observed at 214 km where the strongest T_e enhancements occurred. The total electron content along magnetic field line was calculated in the altitude range from 185 to 325 km and its behaviour is also shown in Fig. 39 (top panel). The well-defined increases are clearly seen in the total electron content from the 15:56–16:06 and 16:16–16:26 UT heater-on cycles. Such electron density enhancements can be attributed to HF-induced ionization production rather than the change of the density distribution due to the thermal diffusion. Note that the experiment was conducted under quiet magnetic conditions, thus any N_e increases due to soft electron precipitation from the magnetosphere could be excluded.

Worth mentioning is that the incoherent backscatter spectra obtained with the EISCAT UHF radar during X-mode HF pumping demonstrate strongly heater-enhanced ion line shoulders and plasma lines, which are unusual for X-mode heating. The heater-enhanced ion and plasma lines are due to the electromagnetic parametric de-

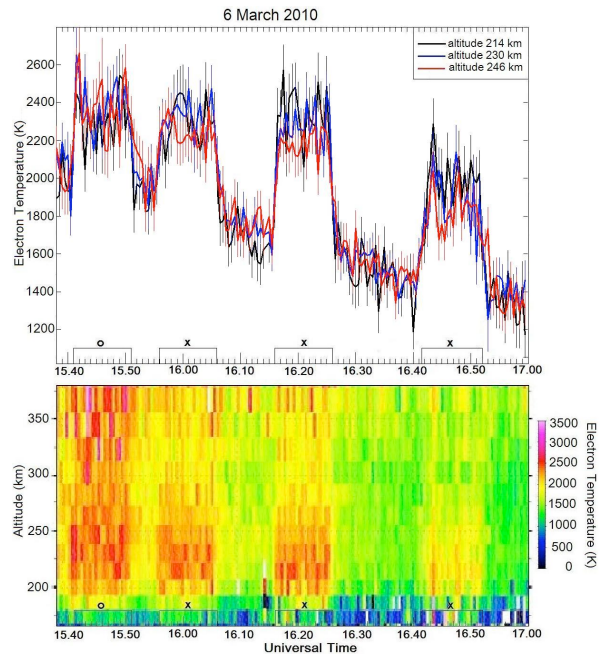


Figure 38: Variations in time of the electron temperature T_e with error-bars at different altitudes (top panel) and its behaviour in the altitude – universal time UT coordinates (bottom panel), obtained from the EISCAT UHF radar observations for contrasting O/X-mode heating on 6 March 2010 from 15:38–17:00 UT. O/X-mode heater-on periods are marked in the time axis.

cay instability (Stubbe, 1996). Behaviour of the downshifted, unshifted, and upshifted ion line amplitudes in the course of the experiment on 6 November 2010 is shown in Figure 40.

The mechanism of the X-mode AFAIs is not clear. Vas'kov and Ryabova (1998) have theoretically shown that the generation process of short wavelength (upper-hybrid and electron cyclotron) plasma oscillations can be produced by induced scattering of a powerful extraordinary HF radio waves by ions. They also note that the high frequency turbulence excited near the reflection level of the powerful extraordinary HF wave leads to the substantial enhancements of low frequency plasma perturbations. The large growth and decay times observed are typical for large-scale ionospheric irregularities with spatial scales of the order of the heated patch (~ 60 km). In such a case one would expect that the behaviour of the small-scale AFAIs, with spatial scales of the order $l_{\perp} \approx 9 - 15$ m, which are responsible for the strong backscattered signals from the CUTLASS measurements, is driven by the large-scale ionospheric irregularities.

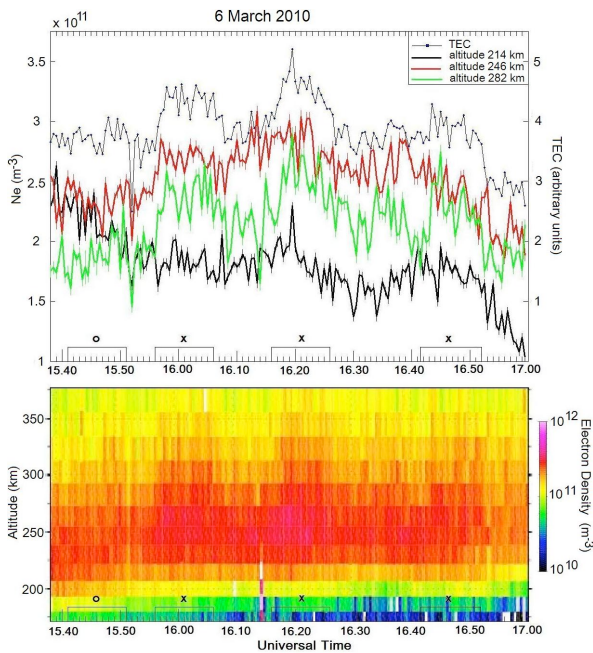


Figure 39: Variations in time of the electron density N_e with error-bars at different altitudes and the total electron content in the altitude range from 180 to 325 km (top panel) and the N_e behaviour in the altitude – universal time UT coordinates (bottom panel), obtained from the EISCAT UHF radar observations for contrasting O/X-mode heating on 6 March, 2010 from 15:38–17:00 UT. O/X-mode heater-on periods are marked in the time axis.

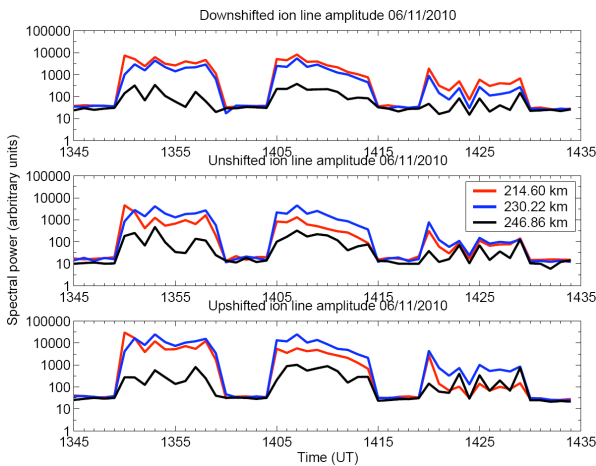


Figure 40: Behaviour of the downshifted, unshifted, and upshifted ion line amplitudes in the course of the experiment on 6 November 2010 from 13:45 to 14:35 UT. HF heating with X-mode of polarization was made from 13:50–14:00, 14:05–14:15, and 14:20–14:30 UT.

N. F. Blagoveshchenskaya, "Phenomena initiated by powerful HF radio waves the high latitude ionosphere:

Results and future plans", *Problems of Arctica and Antarctica* 84, 81–99, (in Russian) 2010.

N. F. Blagoveshchenskaya, et al., "Phenomena in the high latitude ionosphere induced by powerful HF radio waves from EISCAT/Heating facility: Part 1. Peculiarities of excitation and behavior of small-scale artificial field-aligned irregularities and ionospheric plasma features", *Radiophysics & Quant. Electr.* 53, 9–10. 2010.

N. F. Blagoveshchenskaya, et al., "Results from Russian experiments on the impact of powerful HF radio waves in the high latitude ionosphere by using EISCAT facilities", *Solar-Terrest. Physics*, (in press), (in Russian) 2010.

N. F. Blagoveshchenskaya, et al., "Artificial small-scale field-aligned irregularities in the high latitude F region of the ionosphere induced by an X-mode HF heater wave", *Geophys. Res. Lett.*, doi:10.1029/2011GL046724, in press, 2011.

UK studies involving artificial heating

Gustavsson et al. (2010) presented electron temperature variations during an EISCAT experiment when the HF heater was transmitting at frequencies above the peak ionospheric critical frequency. During these HF transmission periods, the electron temperature increased from 2000 K up to 2800 K, and both pump frequency and the polarisation were altered between the pump pulses. The observed temperature variation was compared with numerical solutions to the electron energy equation with ohmic heating, modelling the effect of the radio wave heating on the plasma. The agreement between the observations and the model was found to be good.

Kosch et al. (2010) also studied an interval where HF heating caused strong increases in electron temperature, in this case accompanied by artificially induced ion upwelling. The pump-enhanced electron temperatures reached up to ~ 4000 K at altitudes above 350 km, and ion upwelling reached up to ~ 300 m/s above 500 km altitude. The authors concluded that the pump-induced electron pressure gradient could explain the ion velocity below 450 km. Between 450 and 600 km the electron pressure gradient was found to correlate equally with ion acceleration and ion velocity, representing the transition altitude to free ion acceleration. The electron gas pressure gradient was strong enough to explain ion upwelling, at least up to 600 km altitude. Kosch et al also pointed out that such types of active experiments provide the possibility to estimate the variation

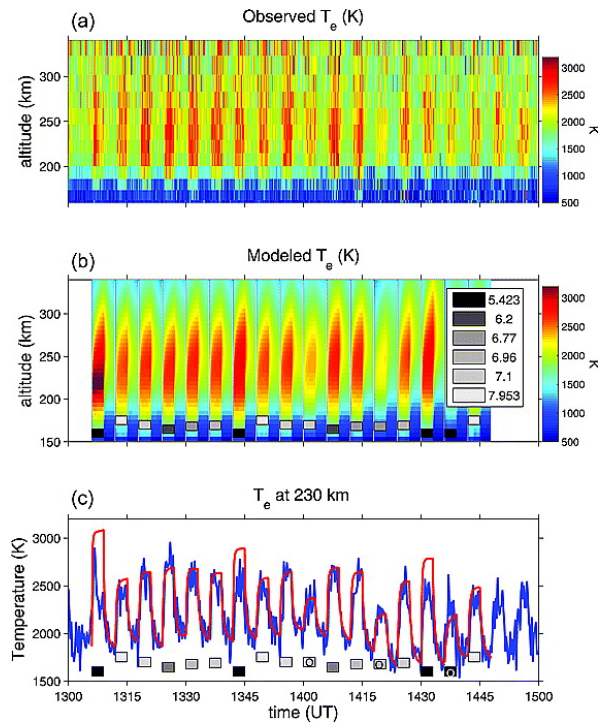


Figure 41: (a) The observed T_e variations agree well with the solution to the electron energy equation with ohmic heating by the HF pump wave; (b) both the temporal characteristics and the variation between different HF pulses, where the pump frequency, power, and polarization varied. (c) It is clearly seen that the only pulse where there is a significant discrepancy between observations (blue curve) and modelling (red curve) results is the first pump period. For this transmission period it is likely that the transmitted frequency was just at or below the X-mode critical frequency, leading to reflection of the pump wave.

of the F layer ion-neutral collision frequency and neutral density with altitude from ground-based observations.

Vickers et al. (2010) presented a study of the spectral features in incoherent scatter data caused by the Purely Growing Mode (PGM), during the first few seconds of EISCAT heating experiments. These features, often referred to as “overshoot” effects, are indicators of turbulent non-Maxwellian plasma, and the analysis of the affected spectra using standard incoherent scatter data analysis software leads to a poor estimation of the plasma parameters, particularly for electron and ion temperature. In this study, the authors developed a procedure to derive a more reliable estimate of plasma temperature during periods when the incoherent scatter spectrum is affected by contamination from the PGM. This was achieved by re-

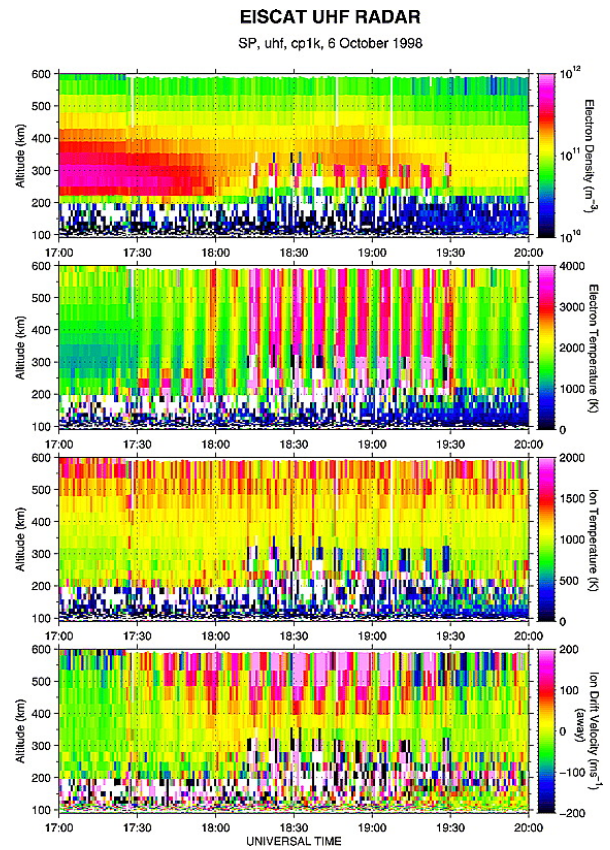


Figure 42: Field-aligned EISCAT UHF radar data for 17–20 UT on 6 October 1998. From top to bottom, the panels show electron density, electron temperature, ion temperature, and ion velocity between 100 and 600 km altitude. The “noisy data” in each panel below ~ 350 km correspond to the pump-induced ion line overshoot phenomenon.

moving the PGM from the measured spectrum and then analysing the modified spectrum using standard software. The results were then compared to those obtained from the analysis of the original, contaminated spectra. It was found that the differences between the results obtained from the corrected and uncorrected spectra were strongly proportional to the magnitude of the PGM feature. Vickers et al. also showed that the bulk temperatures during the remainder of the “heater on” period (after the overshoot) could generally be estimated reliably by the standard analysis software, though with some important exceptions. These results are important since the plasma temperatures play a crucial role in governing thermal conduction processes, and their correct estimation is thus very important to understanding the underlying physical processes which occur during ionospheric heating.

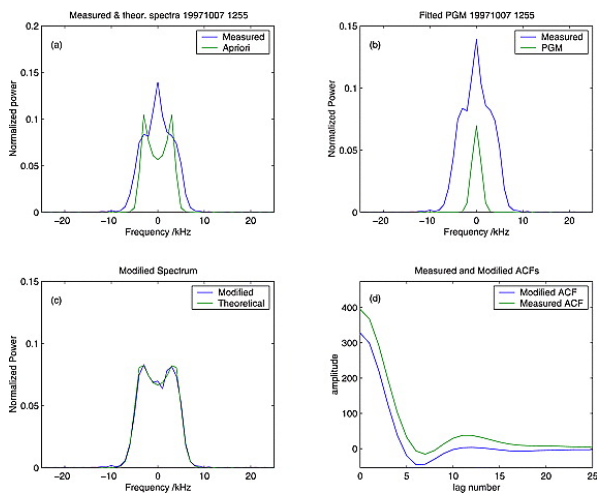


Figure 43: Spectrum correction results for the spectrum at 209 km, at 12:55 UT on 7 October 1997. (a) The measured ion acoustic spectrum (blue) and the a priori theoretical spectrum (green). (b) The measured spectrum (blue) and best fitted Gaussian peak. (c) The fitted theoretical spectrum (green) and the best fit corrected spectrum (blue). (d) The measured ACF (green) and the ACF that results from the Fourier transform of the best fit corrected spectrum.

Radio heating of the free electrons in the mesosphere is an important diagnostic technique for the phenomenon of Polar Mesosphere Summer echoes (PMSE). Due to a lack of suitable observations, the heating must be modelled when studying its effect on PMSE. In order to try to validate these models, Senior et al (2010) implemented a cross-modulation technique on the Tromsø Heater, to compare the absorption of a diagnostic radio wave in the heated and unheated plasma. The results were compared to predictions from a model similar to that used for estimating the heating in PMSE studies. It was found that, after allowing for certain instrumental effects, the model overestimated the change in the absorption of the diagnostic wave by a factor of 1.5–2.5. The authors suggested that the assumption that the electron distribution function remains Maxwellian during heating could contribute to this discrepancy.

Shergill et al. (2010) reported a statistical study of intensity distributions in patches of plasma density irregularities excited by the Tromsø heater during beam-sweeping experiments, and detected by the CUTLASS radar in Finland. During these experiments, the heater beam direction was steadily changed from northward to southward pointing. Comparisons were made between the statistical parameters of the CUTLASS back-

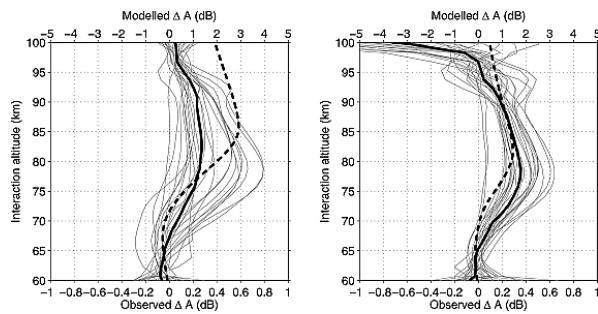


Figure 44: Comparison of observations and modeling for (left) Case 1 and (right) Case 2. The thin gray lines are the diagnostic absorption change profiles for each 60 s sounding. The heavy black line is the median of these profiles; refer to the lower scale. The heavy dashed line is the modelled diagnostic absorption change profile; refer to the upper scale.

catter power distributions and modelled heater beam power distributions. Despite the sometimes seemingly unpredictable nature of the unaveraged results, good agreement was observed between the statistical parameters and the modelled beam, clearly indicating the direct causal connection between the heater beam and the irregularities. The results also gave compelling evidence in support of the upper hybrid theory of irregularity excitation.

B. Gustavsson, et al., "The Rise and Fall of Electron Temperatures I: Ohmic Heating of Ionospheric Electrons from Under-Dense HF-radio Wave Pumping", *J. Geophys. Res.* 115, A12332, doi:10.1029/2010JA015873, 2010.

M. J. Kosch, et al., "An analysis of pump-induced artificial ionospheric ion upwelling at EISCAT", *J. Geophys. Res.* 115, A00I12, doi:10.1029/2010JA015854, 2010.

A. Senior, et al., "Diagnosing Radio Plasma Heating in the Polar Summer Mesosphere using Cross-Modulation: Theory and Observations", *J. Geophys. Res.* 115, A09318, doi:10.1029/2010JA015379, 2010.

H. Shergill, et al., "A statistical study of the spatial distribution of Cooperative UK Twin Located Auroral Sounding System (CUTLASS) backscatter power during EISCAT heater beamsweeping experiments", *J. Geophys. Res.* 115, A05307, doi:10.1029/2009JA014659, 2010.

H. Vickers, et al., "A method for improving plasma temperature estimates from incoherent scatter analysis during artificial ionospheric modification experiments", *J. Geophys. Res.* 115, A11316, doi:10.1029/2010JA015606, 2010.

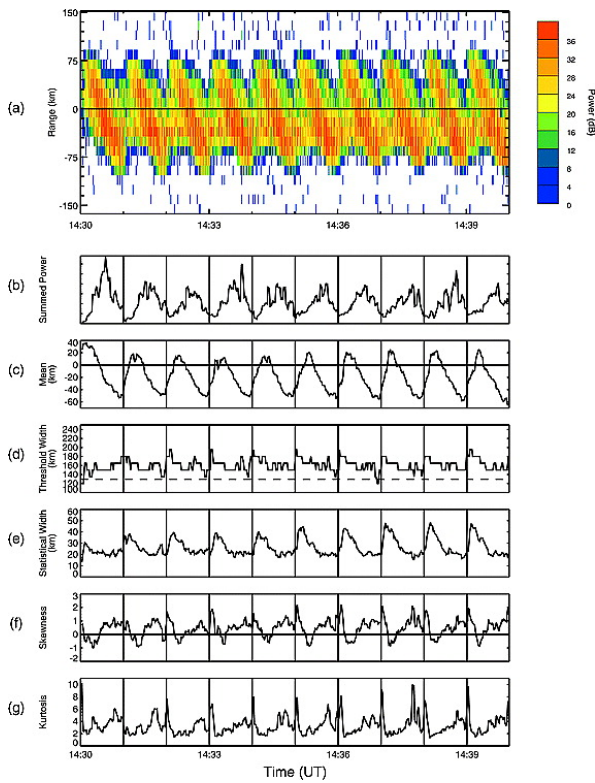


Figure 45: Variation of the statistical parameters of CUTLASS data measured during beam-sweeping run A. Vertical lines indicate the beginning of each sweep, and the horizontal dashed line in panel d represents the upper hybrid width. The horizontal line in panel a indicates the position vertically above the heater.

Inversion results of incoherent scatter spectra

Using powerful HF wave injection the equilibrium of the ionospheric plasma will be modified, that is a non-Maxwellian particle velocity distribution can be produced. The effects of the non-Maxwellian factors and plasma parameters on the spectra characteristics are overlapped and complicated. The ion line spectra near 186 km altitude measured by EISCAT UHF from 9:38 to 11:14 on August 15th 2006, are shown in Fig. 46. The heater was operated at 4.544 MHz, O-mode with a modulation cycle of 4 min on followed by 4 min off and zenith angle 12° (geomagnetic field). Except for a bad data point at 10:54, the incoherent scatter spectra descend, whereas the peak-to-valley ratio of the spectrum line increases during heating. Either the increase of the electron temperature and the non-Maxwellian indices or the decreases of the electron density and ion temperature can result

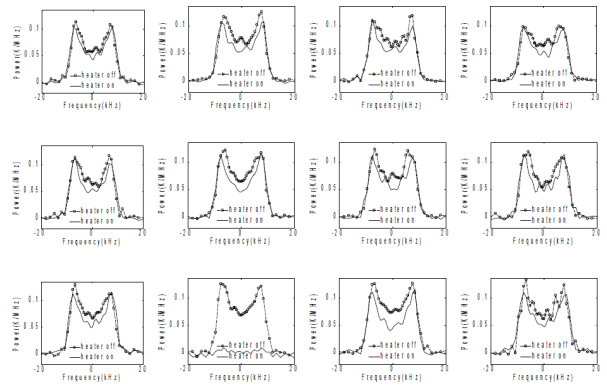


Figure 46: Measurement results of incoherent scatter spectra.

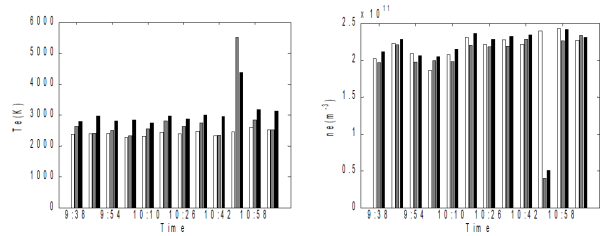


Figure 47: Electron temperature and density during the HF modification experiment (HF off – white; HF on – black: Maxwellian; gray: the irregularities model).

in these modifications. Consequently, the plasma parameters obtained by fitting experimental spectra with the Maxwellian distribution, may be affected.

As shown in Fig. 47, the electron temperature increases up to 27% (627 K), whereas the modification of electron density is very faint. When the heater is on, the electron temperature still clearly increased, but the incremental amplitude is lower than that obtained from standard analysis methods. The standard analysis procedure also overestimate the electron density, which may result in completely erroneous conclusions. In most cases, the reduction of the electron density can be seen in the inversion results from the irregularities model, which is consistent with the prediction of the theoretical model, whereas the phenomenon does not appear in the Maxwellian analysis results.

B. Xu, et al., "The inversion of incoherent scatter spectra with a non-Maxwellian electron distribution", J. Atmos. Terr. Phys. 72, 492–497, 2010.

Spectra of non-Maxwellian distributions

The equilibrium of the ionospheric plasma is modified when using powerful HF wave injection, so that a non-Maxwellian particle velocity distribution may be produced. The non-Maxwellian electron distribution can be described by a superposition of a high temperature distribution and a background distribution

$$f_e = \frac{1-R}{\pi^{1/2}a} \exp(-v^2/a^2) + \frac{R}{\pi^{1/2}v_{th}} \exp(-v^2/v_{th}^2), \quad (1)$$

where $a = \sqrt{2k_B T_e/m_e}$ denotes the thermal velocity of the background electrons, and R the electron density ratio of the high temperature component and the background, T_e the background electrons temperature, m_e the electron mass, k_B the Boltzmann constant, $m = \sqrt{T_e/T_e}$ the irregularities temperature coefficient and $v_{th} = ma$.

By neglecting the magnetic field and collisions, the power spectra are given by

$$S(\mathbf{k}, \omega) = \frac{2\pi}{k} \left| 1 - \frac{G_e}{\varepsilon} \right|^2 f_e \left(\frac{\omega}{k} \right) + \frac{2\pi Z}{k} \left| \frac{G_e}{\varepsilon} \right|^2 f_i \left(\frac{\omega}{k} \right) \quad (2)$$

where \mathbf{k} is the wave vector, Z the charge number of the ions, $\varepsilon = 1 + G_e e + G_e i$ the dielectric function, and G_e and G_i are defined respectively as

$$G_e(\mathbf{k}, \omega) = \int_{-\infty}^{\infty} d\mathbf{v} \frac{4\pi e^2 n_{e0}}{m_e k_B^2} \frac{\mathbf{k} \times \partial f_e / \partial \mathbf{v}}{\omega - \mathbf{k} \times \mathbf{v}} \quad (3)$$

$$G_i(\mathbf{k}, \omega) = \int_{-\infty}^{\infty} d\mathbf{v} \frac{4\pi e^2 n_{i0}}{m_i k_B^2} \frac{\mathbf{k} \times \partial f_i / \partial \mathbf{v}}{\omega - \mathbf{k} \times \mathbf{v}} \quad (4)$$

where f_e is given by Eq. (1).

The effects of the ordinary ionosphere parameters and the non-Maxwellian indices on the incoherent scatter spectra are presented in Fig. 48. With the increase in the electron temperature, the ion resonance frequency increases and the peak-to-valley ratio in the spectrum enhances. With the increase in the ion temperature, however, the peak-to-valley ratio declines, and the spectral width is broadened. The ion resonance frequency and the area increase and the spectral peak becomes sharper as electron density increases. With increase in R , the amplitude of the ion line and the spectral area is reduced while the peak-to-valley ratio enhances. It is clear that effects from the non-Maxwellian factors and from the plasma parameters on the spectra characteristics overlap.

B. Xu, et al., "The inversion of incoherent scatter spectra with a non-Maxwellian electron distribution", *J. Atmos. Terr. Phys.* 72, 492-497, 2010.

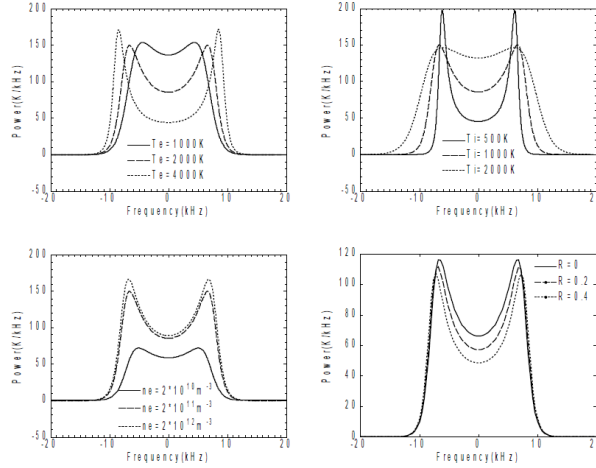


Figure 48: Variation of ISR spectra having non-Maxwellian indices.

New radar techniques

Simulation of post-ADC digital beamforming for large aperture array radars

The feasibility of using a Fractional Sample Delay (FSD) system in the planned EISCAT_3D incoherent scatter radar has been simulated. Key requirements include a frequency-independent beam direction over a 30 MHz band centered around 220 MHz, with correct reconstruction of pulse lengths down to 200 ns. The clock jitter from sample to sample must be extremely low for the integer sample delays. The FSD must also be able to delay the 30 MHz wide signal band by $1/1024^{\text{th}}$ of a sample without introducing phase shifts, and it must operate entirely in baseband. An extensive simulation system based on mathematical models has been developed, with inclusion of performance-degrading aspects such as noise, timing error, and bandwidth. Finite Impulse Response (FIR) filters in the baseband of a bandpass-sampled signal are used to apply true time delay beamforming. It has been confirmed that such use is both possible and well behaved. The target beam-pointing accuracy of 0.06° is achievable using optimized FIR filters with lengths of 36 taps and an 18 bit coefficient resolution (Fig. 49). Even though the minimum fractional delay step necessary for beamforming is ~ 13.1 ps, the maximum sampling timing error allowed in the array is found to be $\sigma \leq 120$ ps if the errors are close to statistically independent.

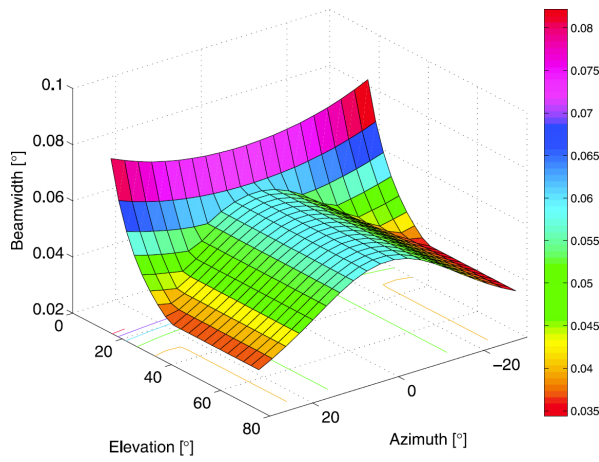


Figure 49: A beam width test run is shown for the 12×4 test array with 120 ps timing error included. The 0.06° maximum beam width demand is met only for elevations above $\sim 20^\circ$. There are barely visible peaks that show the limited but existent effect of a distributed timing error on the beam width.

G. Johansson, et al., "Simulation of post-ADC digital beamforming for large aperture array radars", Radio Sci. 45, RS3001, doi:10.1029/2008RS004124, 2010.

List of publications 2010

- Aruliah, A.L., E.M. Griffin, H.-C. I. Yiu, I. McWhirter, and A. Charalambous, SCANDI an all-sky Doppler imager for studies of thermospheric spatial structure, *Ann. Geophys.*, 28, 549-567, 2010.
- Bin, X., Zhange Wang, Kue Xue, Jian Wu, Zhensen Wu, Jun Wu, Yubo Yan, The inversion of incoherent scatter spectra with a non-Maxwellian electron distribution, *Journal of Atmospheric and Solar-Terrestrial Physics*, 72, 5-6, 492-497, doi:10.1016/j.jastp.2010.01.006, 2010.
- Bisi, M.M., R.A. Fallows, A.R. Breen and I.J. O'Neill, Interplanetary Scintillation Observations of Stream Interaction Regions in the Solar Wind, *Solar Physics*, 261,1, 149-172, DOI: 10.1007/s11207-009-9471-1, 2010.
- Bisi, M.M., A.R. Breen, B.V. Jackson, R.A. Fallows, A.P. Walsh, Z. Mikic, P. Riley, C.J. Owen, A. Gonzalez-Esparza, E. Aguilar-Rodriguez, H. Morgan, E.A. Jensen, A.G. Wood, M. Tokumaru, P.K. Manoharan, I.V. Chashei, A.S. Giunta, J.A. Linker, V.I. Shishov, S.A. Tyul'bashev, G. Agalya, S.K. Glubokova, M.S. Hamilton, K. Fujiki, P.P. Hick, J.M. Clover, and B. Pinter, From the Sun to the Earth: the 13 May 2005 Coronal Mass Ejection, *Solar Physics*, 265, 1-2, 49-127, DOI: 10.1007/s11207-010-9602-8, 2010.
- Bisi, M.M., B.V. Jackson, A.R. Breen, G.D. Dorrian, R.A. Fallows, J.M. Clover and P.P. Hick, Three-Dimensional (3-D) Reconstructions of EISCAT IPS Velocity Data in the Declining Phase of Solar Cycle 23, *Solar Physics*, 265, 1-2, 233-244, DOI: 10.1007/s11207-010-9594-4 , 2010.
- Blagoveshchenskaya N.F., Phenomena initiated by powerful HF radio waves the high latitude ionosphere: Results and future plans. *Problems of Arctica and Ant- arctica*, V.84. N1, pp. 81-99., (in Russian), 2010.
- Blagoveshchenskaya, N.F., T.D. Borisova, M.T. Rietveld, T.K. Yeoman, D.M. Wright, M. Rother, H. Lühr, E.V. Mishin, C. Roth, Results from Russian experiments on the impact of powerful HF radio waves in the high latitude ionosphere by using EISCAT facilities, *Solar- Terrestr. Physics*, (in Russian), (in press) 2010.
- Blagoveshchenskaya N.F., T.D. Borisova, T.K. Yeoman, M.T. Rietveld, Modification of the high latitude ionosphere by powerful HF radio waves. 1. Results from multi-instrument ground-based observations, *Radiophys. & Quant. Electr.*, 53, 9-10, 512-531, DOI: 10.1007/s11141-011-9247-y , 2011. (Translated from *Izvestiya Vysshikh Uchebnykh Zavedenii, Radiofizika*, 53, 9-10, pp. 571-593, September-October 2010.)
- Blelly, P.-L., D. Alcayde, and A.P. van Eyken, A new analysis method for determining polar ionosphere and upper atmosphere characteristics from ESR data: Illustration with IPY period, *J. Geophys. Res.*, 115, A09322, doi:10.1029/2009JA014876, 2010.
- Brosch, N., I. Häggström, A. Pellinen-Wannberg, and A. Westman, Unusual features in high statistics radar meteor studies at EISCAT, *Monthly Notices of Royal Astro- nomical Society*, 401, 2, 1069-1079, 2010.
- Dahlgren, Hanna, Multi-spectral analysis of fine scale aurora, PhD thesis, University of , Sweden, 2010.
- Dorrian, G.D., A.R. Breen, J.A. Davies, A.P. Rouillard, I.C. Whittaker, C.J. Davis, D.S. Brown, R.A. Fallows, R.A. Harrison and M. Grande, Transient structures and stream interaction regions in the solar wind: Results from EISCAT interplanetary scintillation, STEREO HI and Venus Express ASPERA-4 observations, *Solar Physics*, 265, 1-2, 207-231, DOI: 10.1007/s11207-010-9599-z, 2010.
- Gillies, R.G., G.C. Hussey, G.J. Sofko, D.M. Wright, J.A. Davies, A comparison of EISCAT and SuperDARN F-region measurements with consideration of the refractive index in the scattering volume, *J. Geophys. Res.*, 115, A06319, doi:10.1029/2009JA014694, 2010.
- Grydeland, T., and C. La Hoz, Phase calibration of a radar interferometer by means of incoherent scattering, *Radio Sci.*, 45, RS4001, doi:10.1029/2009RS004249, 2010.
- Gustavsson, B., M. T. Rietveld, N. V. Ivchenko, and M. J. Kosch, The Rise and Fall of Electron Temperatures I: Ohmic Heating of Ionospheric Electrons from Under- Dense HF-radio Wave Pumping, *J. Geophys. Res.*, 115, A12332, doi:10.1029/2010JA015873, , 2010.
- Hosokawa, K., Y. Ogawa, A. Kadokura, H. Miyaoka, and N. Sato, Modulation of ionospheric conductance and electric field associated with pulsating aurora, *J. Geophys. Res.*, 115, A03201, doi:10.1029/2009JA014683, 2010.

- Hubert, B., A. T. Aikio, O. Amm, T. Pitkänen, K. Kauristie, S. E. Milan, S. W. H. Cowley, and J.-C. Gérard, Comparison of the open-closed field line boundary location inferred using IMAGE-FUV SI12 images and EISCAT radar observations, *Ann. Geophys.*, 28, 883-892, 2010.
- Johansson, G., J. Borg, J. Johansson, M. Lundberg Nordenvaad, and G. Wannberg, Simulation of post-ADC digital beamforming for large aperture array radars, *Radio Sci.*, 45, RS3001, doi:10.1029/2008RS004124, 2010.
- Kosch, M.J., Y. Ogawa, M.T. Rietveld, S. Nozawa and R. Fujii, An analysis of pump-induced artificial ionospheric ion upwelling at EISCAT, *J. Geophys.*, 115, A12317, doi:10.1029/2010JA015854, 2010.
- Li, Hailong, Jian Wu, Jiying Huang, Maoyan Wang, Reflection characteristics of layered media in polar mesopause occurring polar mesosphere summer echoes, *Plasma Science and Technology*, 12, 4, 416-420, doi:10.1088/1009-0630/12/4/07, Aug. 2010.
- Li, Q., M. Rapp, J. Röttger, R. Latteck, M. Zecha, I. Strelnikova, G. Baumgarten, M. Hervig, C. Hall, and M. Tsutsumi, Microphysical parameters of mesospheric ice clouds derived from calibrated observations of polar mesosphere summer echoes at Bragg wavelengths of 2.8 m and 30 cm, *J. Geophys. Res.*, 115, D00I13, doi:10.1029/2009JD012271, 2010.
- Lorentzen, D. A., J. Moen, K. Oksavik, F. Sigernes, Y. Saito, and M. G. Johnsen (2010), In situ measurement of a newly created polar cap patch, *J. Geophys. Res.*, 115, A12323, doi:10.1029/2010JA015710, 2010.
- Milikh, G. M., A. G. Demekhov, K. Papadopoulos, A. Vartanyan, J. D. Huba, and G. Joyce, Model for artificial ionospheric duct formation due to HF heating, *Geophys. Res. Lett.*, 37, L07803, doi:10.1029/2010GL0426, 2010.
- Nordblad, E. and T.B. Leyser, Ray tracing analysis of L mode pumping of the ionosphere, with implications for the magnetic zenith effect, *Ann. Geophys.*, 28, 1749-1759, 2010.
- Nozawa, S., Y. Ogawa, S. Oyama, H. Fujiwara, T. Tsuda, A. Brekke, C. M. Hall, Y. Murayama, S. Kawamura, H. Miyaoka, and R. Fujii, Tidal waves in the polar lower thermosphere observed using the EISCAT long run data set obtained in September 2005, *J. Geophys. Res.*, 115, A08312, doi:10.1029/2009JA015237, 2010.
- Nygren, T. and Th. Ulich, Calculation of signal spectrum by means of stochastic inversion, *Ann. Geophys.*, 28, 1409-1418, 2010.
- Ogawa, Y., S.C. Buchert, A. Sakurai, S. Nozawa, R. Fujii, Solar activity dependence of ion upflow in the polar ionosphere observed with the European Incoherent Scatter (EISCAT) Tromsø UHF radar, *J. Geophys. Res.*, 115, A07310, doi:10.1029/2009JA014766, 2010.
- Oksavik, K., V. L. Barth, J. Moen, and M. Lester (2010), On the entry and transit of high-density plasma across the polar cap, *J. Geophys. Res.*, 115, A12308, doi:10.1029/2010JA015817, 2010.
- Oyama, S., K. Shiokawa, J. Kurihara, T.T. Tsuda, S. Nozawa, Y. Ogawa, Y. Otsuka, and B. J. Watkins, Lower-thermospheric wind fluctuations measured with an FPI during pulsating aurora at Tromsø Norway, *Ann. Geophys.*, 28, 1847-1857, 2010.
- Rinne, Yvonne, EISCAT Svalbard Radar Studies of Meso-Scale Plasma Flow Channels in the polar cusp ionosphere, PhD thesis, University of Oslo, 2010.
- Rother, M., K. Schlegel, H. Lühr, and D. Cooke, Validation of CHAMP electron temperature measurements by incoherent scatter radar data, *Radio Sci.*, 45, RS6020, doi:10.1029/2010RS004445, 2010.
- Senior, A., M.T. Rietveld, M.J. Kosch and W. Singer, Diagnosing Radio Plasma Heating in the Polar Summer Mesosphere using Cross-Modulation: Theory and Observations, *J. Geophys. Res.*, 115, A09318, doi:10.1029/2010JA015379, 2010.
- Shergill, H., T.R. Robinson, R.S. Dhillon, M. Lester, S.E. Milan, and T.K. Yeoman, A statistical study of the spatial distribution of Cooperative UK Twin Located Auroral Sounding System (CUTLASS) backscatter power during EISCAT heater beamsweeping experiments, *J. Geophys. Res.*, 115, A05307, doi:10.1029/2009JA014659, 2010.
- Strelnikova, I., and M. Rapp, Studies of polar mesosphere summer echoes with the EISCAT VHF and UHF radars: Information contained in the spectral shape, *Adv. Space Res.*, 45, 2, 247-259, doi:10.1016/j.asr.2009.09.007, 2010.
- Vickers, H., T. Robinson, and I. W. McCrea, A method for improving plasma temperature estimates from incoherent scatter analysis during artificial ionospheric modification experiments, *J. Geophys. Res.*, 115, A11316, doi:10.1029/2010JA015606, 2010.
- Voiculescu, M., T. Nygren, A. Aikio, and R. Kuula, An olden but golden EISCAT observation of a quiet-time ionospheric trough, *J. Geophys. Res.*, 115, A10315, doi:10.1029/2010JA015557, 2010.

- Wannberg U.G., Andersson H., Behlke R., Belyey V., Bergqvist P., Borg J., Brekke A., Delsing J., Eliasson L., Finch I., Grydeland T., Gustavsson B., Haggstrom I., Harrison R.A., Iinatti T., Johansson G., Johansson J., Johansson J., La Hoz C., Laakso T., Larsen R., Larsmark M., Lindgren T., Lundberg M., Markkanen J., Marttala I., McCrea L., McKay D., Postila M., Puccio W., Renkwitz T., Turunen E., van Eyken A., Vanhainen L.-G., Westman A. and Wolf I., EISCAT_3D - A next-generation European radar system for upper atmosphere and geospace research, *Radio Science Bulletin*, No 332, 75-88, 2010
- Wild, P., F. Honary, A. J. Kavanagh, and A. Senior, Triangulating the height of cosmic noise absorption: A method for estimating the characteristic energy of precipitating electrons, *J. Geophys. Res.*, 115, A12326, doi:10.1029/2010JA015766., 2010.
- Wood, A. G. and Pryse, S. E., Seasonal influence on polar cap patches in the high-latitude nightside ionosphere, *J. Geophys. Res.*, 115, A07311, doi:10.1029/2009JA014985, 2010.
- Woodfield, E. E., J. A. Wild, A. J. Kavanagh, A. Senior, and S. E. Milan, Combining incoherent scatter radar data and IRI-2007 to monitor the open-closed field line boundary during substorms, *J. Geophys. Res.*, 115, A00I15, doi:10.1029/2010JA015751, 2010.
- Xue Kun, Wu Jian, Xu Bin, Guo Lixin, Interpretation on the origin of enhanced ion acoustic line spectra in the high ionosphere, *Chin. J. Space Sci.*, 30(1), 29-34 (in Chinese), 2010.
- Xu Bin, Wang Zhange, Xu Zhengwen, Wu Zhensen, Wu Jian, Wu Jun, Xue Kun, Che Haiqing, Yan Yubo, Observations of the heating experiments in the polar winter ionosphere - Analysis in low region. *Chinese Journal Geophysics*, 53(6), 1263-1268 (in Chinese), 2010.
- Xu Bin, Wu Zhensen, Wu Jian, Che Haiqing, Wu Jun, Xue Kun, 2D numerical simulation of the artificial ionospheric modification in polar region, *Chinese Journal of Radio Science*, 25(1), 14-19, (in Chinese), 2010.
- Xu Bin, Wang Zhange, Wu jun, Xu Zhengwen, Xue Kun, Wu Jian, Observation of The Heating Experiments in the Polar Ionosphere in August, 2009, *Chinese Journal of Polar Research*, 22, 4, 334-347, DOI: 10.3724/SPJ.1084.2010.00334, (in Chinese), 2010.
- Zhang, S.-R., J.M. Holt, A.P. van Eyken, C. Heinselman, and M. McCready, IPY observations of ionospheric yearly variations from high- to middle-latitude incoherent scatter radars, *J. Geophys. Res.*, 115, A03303, doi:10.1029/2009JA014327, 2010.

EISCAT Operations 2010

The EISCAT radars operate in two basic modes, using approximately half the available observing time for each. In the Special Programme mode, users conduct individual experiments dedicated to specific experiments and objectives. The resulting data are reserved for the exclusive use of the experimenters for one year from the date of collection. Special programmes often make use of the well developed pulse schemes and observing modes of the Common Programme. EISCAT Common Programmes are conducted for the benefit of the entire user community and the resulting data are immediately available to all. The Common Programme modes are developed and maintained by EISCAT staff, and the overall programme is monitored by the Scientific Oversight Committee (SOC). Common Programme operations are often conducted as part of the coordinated World Day programme organised by the International Union of Radio Scientists (URSI) Incoherent Scatter Working Group (ISWG).

Common Programme One, CP-1, uses a fixed transmitting antenna, pointing along the geomagnetic field direction. The three-dimensional velocity and anisotropy in other parameters are measured by means of the receiving stations at Kiruna and Sodankylä (see map, inside front cover). CP-1 is capable of providing results with very good time resolution and is suitable for the study of substorm phenomena, particularly auroral processes where conditions might change rapidly. The basic time resolution is 5 s. Continuous electric field measurements are derived from the tri-static F-region data. On longer time scales, CP-1 measurements support studies of diurnal changes, such as atmospheric tides, as well as seasonal and solar-cycle variations. The observation scheme uses alternating codes for spectral measurements.

Common Programme Two, CP-2, is designed to make measurements from a small, rapid transmitter antenna scan. One aim is to identify wave-like phenomena with length and time scales comparable with, or larger than, the scan (a few tens of kilometers and about ten minutes). The present version consists of a four-position scan which is



EISCAT Svalbard radar antennas.

completed in six minutes. The first three positions form a triangle with vertical, south, and south-east positions, while the fourth is aligned with the geomagnetic field. The remote site antennas provide three-dimensional velocity measurements in the F-region. The pulse scheme is identical with that of CP-1.

Common Programme Three, CP-3, covers a 10° latitudinal range in the F-region with a 17-position scan up to 74°N in a 30 minute cycle. The observations are made in a plane defined by the magnetic meridian through Tromsø, with the remote site antennas making continuous measurements at 275 km altitude. The coding scheme uses alternating codes. The principle aim of CP-3 is the mapping of ionospheric and electrodynamic parameters over a broad latitude range.

Common Programmes One, Two, and Three are run on the UHF radar. Three further programmes are designed for use with the VHF system. The UHF and VHF radars are often operated simultaneously during the CP experiments. Such observations offer comprehensive data sets for atmospheric, ionospheric, and magnetospheric studies.

Common Programme Four, CP-4, covers geographic latitudes up to almost 80°N (77°N invariant latitude) using a low elevation, split-beam configuration. CP-4 is particularly suitable for studies of high latitude plasma convection and polar cap phenomena. However, with the present one-beam



EISCAT VHF and UHF transmitter antennas, Tromsø.

configuration of the VHF radar, CP-4 is run with either both UHF and VHF radars or with UHF only in a two position scan.

Common Programme Six, CP-6, is designed for low altitude studies, providing spectral measurements at mesospheric heights. Velocity and electron density are derived from the measurements and the spectra contain information on the aeronomy of the mesosphere. Vertical antenna pointing is used.

Common Programme Seven, CP-7, probes high altitudes and is particularly aimed at polar wind studies. The present version, with only one of the VHF klystrons running, is designed to cover altitudes up to 1500 km vertically above Ramfjordmoen.

Equivalent Common Programme modes are available for the EISCAT Svalbard Radar. CP-1

is directed along the geomagnetic field (81.6° inclination). CP-2 uses a four position scan. CP-3 is a 15 position elevation scan with southerly beam swinging positions. CP-4 combines observations in the F-region viewing area with field-aligned and vertical measurements. Alternating code pulse schemes have been used extensively for each mode to cover ranges of approximately 80 to 1200 km with integral clutter removal below 150 km. CP-6 is similar to the mainland radar CP-6.

The tables on the next pages summarise the accounted hours on the various facilities for each month and for each Common Programme mode (CP) or Associate (SP).

*Dr. Ingemar Häggström
Senior Scientist, EISCAT Scientific Association*

KST COMMON PROGRAMMES

2010	Jan	Feb	Mar	Apr	May	Jun	Jul	Aug	Sept	Oct	Nov	Dec	Total	%	Target%
CP1		5.5	94.5	39.5	39				12	60.5	59.5		310.5	30	16
CP2	413.5												413.5	40	16
CP3													0	0	12
CP4													0	0	10
CP6	36.5			5.5			36	37.5	1				116.5	11	20
CP7						63			63			62	188	18	18
UP1													0	0	
UP2													0	0	
UP3													0	0	
Total	450	5.5	94.5	45	39	63	36	37.5	76	60.5	59.5	62	1028.5	100	
%	44	1	9	4	4	6	4	4	7	6	6	6		100	

KST SPECIAL PROGRAMMES

2010	Jan	Feb	Mar	Apr	May	Jun	Jul	Aug	Sept	Oct	Nov	Dec	Total	Incl AA	Target
CN			43				19.5		30.5				93	94	84
FI						32.5						164.5	197	199	143
GE												107.5	107.5	109	82
NI	22.5		26							12	96.5		157	160	168
NO			16.5			97.5	3.5						117.5	123	325
SW	31.5	18.5	6							12	40.5		108.5	112	234
UK		53.5					24	3	110		24	39	253.5	257	219
AA								11.5	9				20.5		
Total	54	72	91.5	0	0	130	47	14.5	149.5	24	161	311	1054.5	1055	1256
%	5	7	9	0	0	12	4	1	14	2	15	29		100	

	EI	CN	FI	GE	NI	NO	SW	UK
Target		6.7	11.4	6.56	13.41	25.91	18.6	17.43

KST OTHER PROGRAMMES

2010	Jan	Feb	Mar	Apr	May	Jun	Jul	Aug	Sept	Oct	Nov	Dec	Total	Target
3P													0	35
EI		5.5										3.5	9	25
RU		1.5	60									60.5	122	139
TB			13.5									3.5	24	41
Total	0	7	73.5	0	0	0	0	0	0	0	0	64	172	240

KST CUMULATIVE TOTALS

2010	Jan	Feb	Mar	Apr	May	Jun	Jul	Aug	Sept	Oct	Nov	Dec	Total	Target
CP	450	5.5	94.5	45	39	63	36	37.5	76	60.5	59.5	62	1028.5	840
SP	54	72	91.5	0	0	130	47	14.5	149.5	24	161	311	1054.5	1256
OP	0	7	73.5	0	0	0	0	0	0	0	0	64	172	240
Total	504	84.5	259.5	45	39	193	83	52	225.5	84.5	284.5	400.5	2255	2335

USAGE BREAKDOWN

2010	Jan	Feb	Mar	Apr	May	Jun	Jul	Aug	Sept	Oct	Nov	Dec	Total	Target
UHF	309.5	42.5	158.5	0.5		57	19.5		60	41	157.5	119.5	965.5	984
VHF	41	10.6		44.5	39	92	53	49.5	84	24	46	229	712.6	747
Heating		13	43.5			37			53		43.5	29	219	254
Passive UHF	618	51	228			26		11.5	114.5	77.5	149.5	94.5	1370.5	1400
ESR	253.5	50.5	82	91	67	64	41.5	53	74	102.5	178	166.5	1223.5	1406
Passive ESR								6	64				70	

ESR COMMON PROGRAMMES

2010	Jan	Feb	Mar	Apr	May	Jun	Jul	Aug	Sept	Oct	Nov	Dec	Total	%	Target%
CP1	1.5	2	62.5	39	39		24.5	30.5	3	39	39		280	43	54
CP2	185												185	28	16
CP3													0	0	12
CP4													0	0	10
CP6													0	0	
CP7						62			63			64	189	29	
UP1													0	0	
UP2													0	0	
UP3													0	0	
Total	186.5	2	62.5	39	39	62	24.5	30.5	66	39	39	64	654	100	
%	29	0	10	6	6	9	4	5	10	6	6	10	100		

ESR SPECIAL PROGRAMMES

2010	Jan	Feb	Mar	Apr	May	Jun	Jul	Aug	Sept	Oct	Nov	Dec	Total	Incl AA	Target
CN													0	1	37
FI											41	22.5	63.5	66	63
GE													0	1	36
NI	13.5							10			22	10.5	56	59	74
NO	5	16	19.5	52		2	17			24	2.5	16	154	159	144
SW	17				24.5						3.5	9	54	58	103
UK	31.5	23.5						1.5	16		3	44.5	120	124	97
AA								12.5	8				20.5		
Total	67	39.5	19.5	52	24.5	2	17	24	24	24	72	102.5	468	468	554
%	14	8	4	11	5	0	4	5	5	5	15	22	100		

ESR OTHER PROGRAMMES

2010	Jan	Feb	Mar	Apr	May	Jun	Jul	Aug	Sept	Oct	Nov	Dec	Total	Target
3P											27.5		27.5	35
EI													0	25
RU			9										9	9
TB						3.5				12	67		82.5	83
Total	0	9	0	0	3.5	0	0	0	0	39.5	67	0	119	152

ESR CUMULATIVE TOTALS

2010	Jan	Feb	Mar	Apr	May	Jun	Jul	Aug	Sept	Oct	Nov	Dec	Total	Target
CP	186.5	2	62.5	39	39	62	24.5	30.5	66	39	39	64	654	700
SP	67	39.5	19.5	52	24.5	2	17	24	24	24	72	102.5	468	554
OP	0	9	0	0	3.5	0	0	0	0	39.5	67	0	119	152
Total	253.5	50.5	82	91	67	64	41.5	54.5	90	102.5	178	166.5	1241	1406

List of meetings 2010

EISCAT Annual Review Meeting

ARM 2010 15–17 March, 2010, Björkliden, Sweden

EISCAT Council

Council 74th 3–4 June 2010, National Institute of Polar Research, Tokyo, Japan

Council 75th 1–2 November 2010, British Antarctic Survey, Cambridge, UK

EISCAT Council Advisory Group

CAG 6th 26 April 2010, Vetenskapsrådet, Stockholm, Sweden

CAG 7th 2–5 October 2010, Finnish Meteorological Institute, Helsinki, Finland

EISCAT Scientific Oversight Committee

SOC 6th 25–26 March 2010, Solar-Terrestrial Environment Laboratory, Nagoya University, Nagoya, Japan

SOC 7th 9–10 September 2010, Arctic and Antarctic Research Institute, St. Petersburg, Russia

EISCAT_3D_2 Preparatory Phase Project Meetings

GA1 6 October 2010, 1st General Assembly meeting of the EISCAT_3D_2 Preparatory Phase project, Radisson Blu Hotel Arlandia, Arlanda, Sweden

EB1 21 October 2010, 1st Executive Board meeting, Clarion Hotel, Stockholm, Sweden

Kick-off 21–22 October 2010, Kick-off meeting for the Preparatory Phase project, Clarion Hotel, Stockholm, Sweden

Weekly Starting from 29 October 2010, weekly Executive Board teleconferences

Staff celebrations 2010

ARM 2010

2 years (Silver pin) Elisabet Goth, Headquarters

5 years (Gold pin) Martin Langteigen, EISCAT
Svalbard Radar

20 years (Wrist watch) Inge Marttala, Kiruna site

25 years (Glass sculpture) Toivo Iinatti, Sodankylä site

Other

Retiring Inge Marttala, Kiruna site
Tarmo Laakso, Sodankylä site

Beynon medals



The EISCAT Council awards distinguished persons the Sir Granville Beynon medal.

Recipients

1st Prof. Tor Hagfors 2002 Awarded to Professor Tor Hagfors on 4th February 2002 for his outstanding services to the EISCAT Scientific Association and to Ionospheric Physics

2nd Prof. Tauno Turunen 2003 In recognition of important contributions to the techniques of Incoherent Scatter Radar and outstanding services to the EISCAT Scientific Association

3rd Prof. Jürgen Röttger 2004 In recognition of outstanding services to the EISCAT Scientific Association including the establishment of the EISCAT Svalbard Radar at Longyearbyen

4th Prof. Henry Rishbeth 2006 Awarded by the Council of the EISCAT Scientific Association to Professor Henry Rishbeth. In recognition of

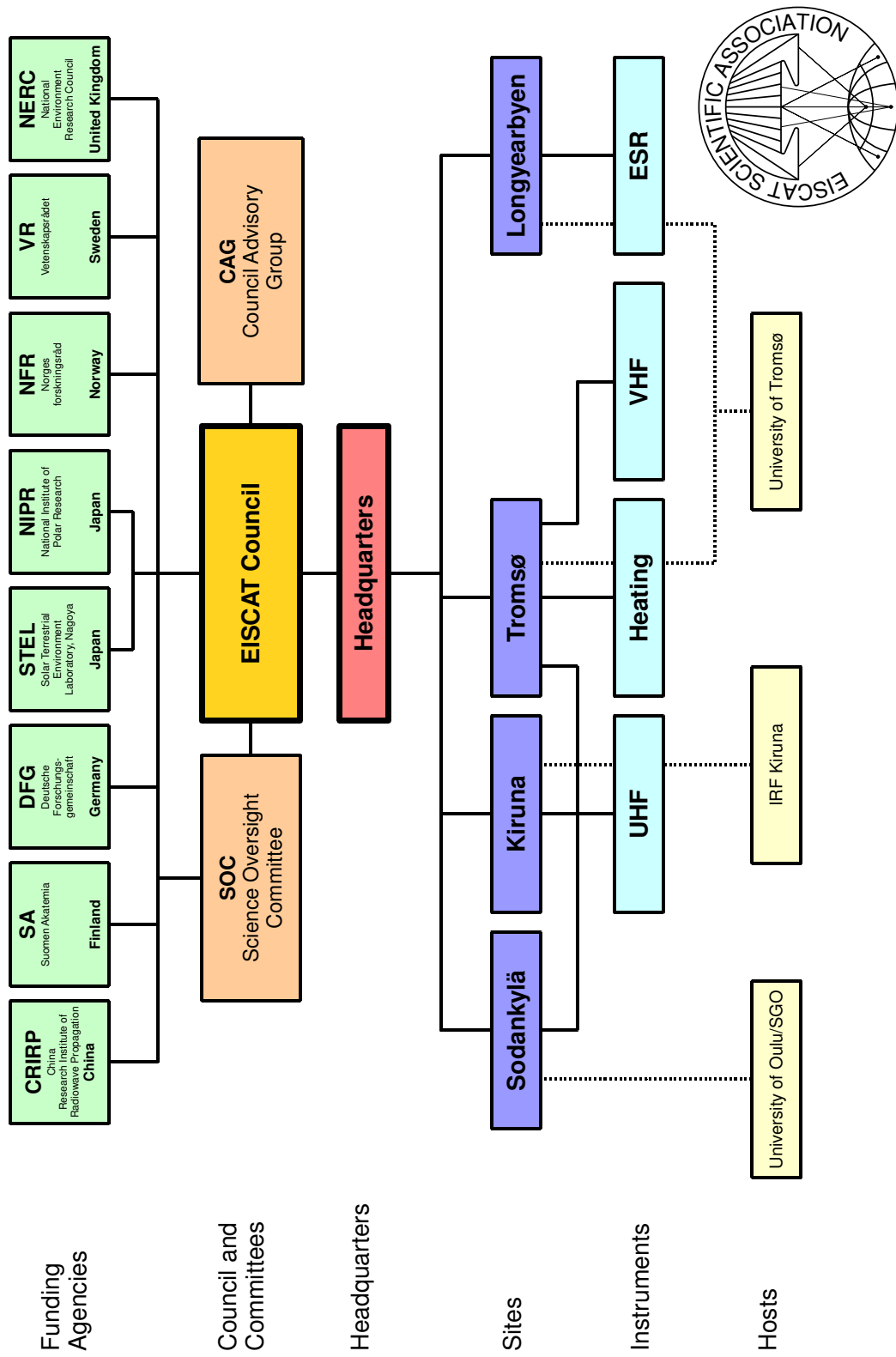
outstanding contributions to the scientific exploitation of incoherent scatter in Europe including the UK PUSCAT and MISCAT radars and the radars of the EISCAT Scientific Association

5th Prof. Nobuo Matuura 2007 Awarded by the Council of the EISCAT Scientific Association to Professor Nobuo Matuura. In recognition of his contributions to the successful establishment of the EISCAT Svalbard Radar at Longyearbyen and to the expansion of the EISCAT Scientific Association to include non-European members

6th Prof. Markku Lehtinen 2008 Awarded by the Council of the EISCAT Scientific Association to Professor Markku Lehtinen. In recognition of his seminal contributions to the development of advanced modulation techniques for incoherent scatter radars and to the mathematical foundations and implementation of effective incoherent scatter radar data analysis systems

7th Dr. Gudmund Wannberg 2009 Awarded by the Council of the EISCAT Scientific Association to Doctor Gudmund Wannberg. In recognition of his persistent work for the technical development of EISCAT radars and his invaluable contribution to the EU Design Study project for the EISCAT_3D radars.

8th Prof. Asgeir Brekke 2010 Awarded by the Council of the EISCAT Scientific Association to Professor Asgeir Brekke in recognition of his pioneering work in polar ionosphere investigations with Incoherent Scatter Radar measurements and of his long-term efforts in advocating EISCAT research worldwide.



EISCAT organisational diagram, December 2010.

EISCAT Scientific Association

December 2010

Council

The Council consists of a Delegation with a maximum of three persons from each Associate.

P. R. of China

Prof. Q. Dong
Prof. J. Wu Delegate

Finland

Dr. A. Aikio
Dr. K. Kauristie *Chairperson*
Dr. K. Sulonen Delegate

Germany

Prof. J. Röttger
Dr. K. Zach Delegate

Japan

Dr. H. Miyaoka Delegate
Dr. S. Nozawa

Norway

Prof. A. Brekke
Dr. B. Jacobsen Delegate
Dr. L. Lønnum

Sweden

Dr. T. Andersson *Vice-Chairperson, Delegate*
Prof. D. Murtagh

United Kingdom

Dr. I. McCrea
Dr. M. Schultz Delegate

Scientific Oversight Committee

The EISCAT scientific community organises the Scientific Oversight Committee (SOC), under the guidance of the Council.

Dr. N. Blagoveshchenskaya	External member
Dr. S. Buchert	Sweden
Dr. J. Chau	External member
Dr. M. Kosch	United Kingdom
Prof. C. La Hoz	Norway
Prof. R. Liu	<i>Chairperson, P. R. of China</i>
Dr. Y. Ogawa	Japan
Prof. M. Rapp	Germany
Dr. T. Ulich	Finland

Director

Dr. E. Turunen

Council Advisory Group

The Council Advisory Group (CAG) prepares matters to be brought to the Council.

Mr. H. Andersson	Head of Administration
Dr. T. Andersson	Council Vice-Chairperson
Prof. A. Brekke	Council Member
Dr. K. Kauristie	Council Chairperson
Dr. I. McCrea	Council Member
Dr. E. Turunen	Director

Executives

Senior Management

Mr. H. Andersson	Head of Adm., Deputy Dir.
Dr. E. Turunen	Director

Site Leaders

Station Managers

Mr. H. Boholm	EISCAT Svalbard Radar
Mr. R. Jacobsen	Tromsø Radar
Mr. J. Markkanen	Sodankylä Site
Dr. M. Rietveld	Tromsø Heating
Mr. L.-G. Vanhainen	Kiruna Site



EISCAT staff at the Annual Review Meeting, 15–17 March 2010, at Björkliden, Sweden.

Appendix:

**EISCAT Scientific Association
Annual Report, 2010**

EISCAT Scientific Association Annual Report 2010

EISCAT Scientific Association
Registered as a Swedish non-profit organisation
Organisation number: 897300-2549

Annual report for the financial year 2010-01-01 – 2010-12-31

The EISCAT Council and the Director for the Association submits herewith the annual report for 2010.

Content	Page
Administration report	1
Profit and loss accounts	5
Balance sheet	6
Statement of cash flows	7
Notes	8

ADMINISTRATION REPORT

Ownership, organisation and objective

The EISCAT Scientific Association was established in 1975 through an agreement between six European organisations. Japan joined in 1996 and the Peoples Republic of China in 2007.

The EISCAT Associates at 2010-12-31 are: China Research Institute of Radiowave Propagation (Peoples Republic of China), Deutsche Forschungsgemeinschaft (Germany), National Institute of Polar Research (Japan), Natural Environment Research Council (United Kingdom of Great Britain and Northern Ireland), Norges forskningsråd (Norway), Solar-Terrestrial Environment Laboratory, Nagoya University (Japan), Suomen Akatemia (Finland), and Vetenskapsrådet (Sweden).

A new EISCAT Agreement came into force 2007-01-01, with all Associates making long term funding commitments to the Association. The Association has its formal seat in Kiruna, Sweden, and is registered as a non-profit organisation.

The aim of the Association is to make significant progress in the understanding of physical processes in the high latitude atmosphere by means of experimental programmes generally conducted using the incoherent scatter radar technique, which may be carried out as part of wider international projects. For this purpose, the Association has developed, constructed, and now operates, a number of radar facilities at high latitudes. At present, these comprise a system of stations at Tromsø (Norway), Kiruna (Sweden), Sodankylä (Finland), and Longyearbyen (Svalbard).

The Association is fully funded by the Associates but additional operations may also be funded by short term additional contributions from both Associate and non-Associate bodies. Depending on the available funding, scientific priorities and operational targets are adjusted on an annual basis.

The EISCAT Council is charged with the overall administration and supervision of the Association's activities. The Council appoints a Director, who is responsible for the daily management and operation of the facilities of the Association.

Operation and scientific development

The EISCAT Radars delivered a full programme of operations for the user community and operated reliably throughout the year with only minor interruptions due to equipment or operational problems.

The various EISCAT radars operated for a total of 3 496 accounted hours (3 688 hours in 2009).

The UHF tristatic runs, first envisaged to not be possible after July 2010, could continue also after that date since the mobile operators that bought that frequency allocation did not start using it during the year. Consequently, some Common Programmes as well as Special

Programme could be run in the tristatic mode (transmit/receive in Tromsø and receive only in Kiruna and Sodankylä).

Common Programmes amounted to 42% (43%) of the operations. Special Programmes amounted to 37% (40%) and other operations amounted to 21% (17%) of the total hours.

Scientists from France, Ukraine and Russia paid for the use of the facilities. Totally 254.5 hours (298.5 hours) were run on behalf of these countries. Both Ukraine and Russia have Affiliate agreements. Additionally, the European Space Agency (ESA) used the infrastructure for a coordinated tracking campaign of objects PROBA-1, METOP-A, JASON_2, GRACE-1, ENVISAT and CRYOSAT_2 in November and December. Totally 28.27 hours were run on behalf of, and paid by, ESA.

The EISCAT_3D planning continued during the year and the EU Framework Programme 7 bid for a preparatory phase, submitted in December 2009, was successful such that a new EU supported project, the FP7 EISCAT_3D_2 preparatory phase could start 2010-10-01. It is a four year project with a total budget volume of 6 MEUR and eight partners. EISCAT is both a partner and coordinator for the project. The budgeted expected support from EU for the EISCAT involvement amounts to 1.25 MEUR spread over the four years. The EU grant for the whole project is 4.5 MEUR, which is channelled through the coordinator.

The goal of the preparatory phase project is to resolve the remaining legal, financial and technical questions which must be addressed before the construction of the EISCAT_3D system.

A new development undertaken in the year was the project proposed by the Chinese Associate, China Research Institute of Radiowave Propagation (CRIRP), to build a third antenna system on Svalbard with dual mode capabilities. The antenna would be used for EISCAT regular radar use and for Chinese operations such as coordinated VLBI measurements together with mainland China antennas. The EISCAT involvement is to do the initial feasibility studies for a possible build on Svalbard. The work is contracted out to consultants and the cost is reimbursed from CRIRP.

Future operation and scientific development

During 2011, EISCAT will continue to support the wide range of existing and new programmes proposed by the various Associates' scientific communities, including the hosting of user-supplied equipment.

Tristatic runs will likely be possible to be done some more months and will be encouraged. The small Demonstrator receive-only array built in connection with the previous EISCAT_3D project, the design study, will be tilted downwards such that the array points at the E region and meteor heights 80-120 km instead of its present direction to F-region around 300 km above the VHF transmitter in Tromsø. If the sensitivity is adequate, it could be a valuable option for many users with interest in the lower regions. The modification will be ready summer 2011.

The three other radar systems, UHF in monostatic mode, VHF and the Svalbard Radar continues undisturbed. The Heating facility has been modernised and can also now be used as a magnetospheric radar.

The work of the Council and its committees

The Council had two ordinary meetings under the leadership of the Chairperson, Dr. Kirsti Kauristie: in June, Tokyo, Japan and in November, Cambridge, United Kingdom. At the end of year, the Council Chairpersonship was taken over by Dr. Tomas Andersson, Vetenskapsrådet, Sweden. He will serve for two years. The Council Advisory Group had two meetings under the leadership of the Chairperson, Dr. Kirsti Kauristie: in April, Stockholm, Sweden and in October, Helsinki, Finland. The Scientific Oversight Committee had two meetings under the leadership of the Chairperson, Prof. Ruiyuan Liu: in March, Nagoya, Japan and in September, St. Petersburg, Russia,

Council considered regular business matters, including the continued EISCAT_3D work and the third antenna proposal. Council decided also to assign 200 hours peer-reviewed pool of time (PP programme) opened for users around the world and to allocate 100 kSEK annually for a regularly occurring radar school. Both actions were implemented in the 2011 budget. The financial implications from potential departure of Associates in 2012 resulted in proactive measures both involving work in improving the income side as well as reducing operating costs to be included in the 2012 budget onwards.

The transfer of the UK Associateship from the Science and Technology Facilities Council (STFC) to the Natural Environment Research Council (NERC) was finalised during the first months of the year meaning that NERC is from 2010-01-01 the UK Associate.

Budget development during the year

The 2010 operations ended just below the operating target set for the year and the operations went without any major technical issues. The application for the EISCAT_3D preparatory phase was done partially by external writers, paid as consultancy. The management travel continued at a very high rate. Income from bank interest continued on a low level. Active placements generated reasonable return that compensated from the marginal bank interest income. The income side continued to benefit from the relatively weak SEK-currency and generated, due to the Associate commitments in local currencies and annual payments in the first half of the year, additional income. The strengthening of SEK during the latter part of the year created though some exchange rate losses.

The long-term budget plan

The long-term budget plan is difficult due to the current known funding shortage from 2012 onwards. For 2011, we plan for a normal year and the overall operating target can likely be maintained. The 2012 budget will include substantial cost reductions, including a reduced staff complement, and the operations from then on will be more directly tied to received contributions.

The result for 2010 and the deficit handling

The year was balanced by covering the deficit, -83 kSEK, from the Restructuring reserve.

PROFIT AND LOSS ACCOUNTS

in thousands of Swedish Crowns

	Note 1	2010	2009
Associate contributions	Note 2	24 248	26 586
Other operating income		3 219	6 180
		<u>27 467</u>	<u>32 766</u>
Operation costs		-6 243	-5 257
Administration costs		-4 413	-4 517
Personnel costs	Note 3	-17 854	-17 706
Depreciation of fixed assets		-1 214	-2 198
		<u>-29 724</u>	<u>-29 677</u>
<i>Operating profit/loss</i>		-2 257	3 089
Interest income		52	85
Other financial income and cost		-41	-622
Own reserves and funds	Note 4	949	-1 335
		<u>960</u>	<u>-1 871</u>
<i>Profit/loss after financial items</i>		-1 297	1 217
Appropriations	Note 5	83	-3 415
Transfer from funds invested	Note 6	1 214	2 198
		<u>1 297</u>	<u>-1 217</u>
<i>Net profit/loss for the year</i>		0	0

BALANCE SHEET

in thousands of Swedish Crowns

		2010	2009
ASSETS			
<u>Fixed assets</u>			
<i>Tangible fixed assets</i>	Note 7		
Buildings		3 557	3 843
Radar systems		748	821
Equipment and tools		1 664	2 099
		<u>5 968</u>	<u>6 764</u>
<u>Current assets</u>			
Receivables		3 050	3 871
Prepayments and accrued income	Note 8	1 129	640
Cash at bank and in hand	Note 9	24 711	19 222
		<u>28 889</u>	<u>23 733</u>
<i>Total assets</i>		34 858	30 496
CAPITAL AND LIABILITIES			
<u>Capital</u>			
Funds invested	Note 10	5 968	6 764
Funds held on reserve	Note 11	17 312	18 763
		<u>23 280</u>	<u>25 526</u>
<u>Long term liabilities</u>			
Long term liabilities	Note 12	0	0
<u>Current liabilities</u>			
Liabilities, trade	Note 13	11 425	4 469
Provisions	Note 14	0	155
Other liabilities		152	345
		<u>11 578</u>	<u>4 970</u>
<i>Total capital and liabilities</i>		34 858	30 496
<i>Pledged assets</i>		<i>0</i>	<i>0</i>
<i>Contingent liabilities</i>		<i>none</i>	<i>none</i>

STATEMENT OF CASH FLOWS

in thousands of Swedish Crowns

	2010	2009
<u>Operating activities</u>		
Operating result before financial items	-2 257	3 089
Transfer from funds invested	1 214	2 198
Interest received	52	85
Currency exchange rate changes	-57	-658
Extra ordinary income and cost	15	36
Increase/decrease of receivables	821	-2 148
Increase/decrease of prepayments and accrued income	-489	-30
Increase/decrease of creditors and liabilities	6 608	-2 252
<i>Cash flow from operations</i>	<i>5 907</i>	<i>321</i>
<u>Investment activities</u>		
Investments in tangible assets	-419	-1 469
<i>Cash flow from investment activities</i>	<i>-419</i>	<i>-1 469</i>
<i>Cash flow for the year</i>	<i>5 488</i>	<i>-1 148</i>
<i>Liquid assets at the beginning of the year</i>	<i>19 222</i>	<i>20 370</i>
<i>Liquid assets at the end of the year</i>	<i>24 711</i>	<i>19 222</i>

EISCAT Scientific Association Annual Report 2010

NOTES

Note 1 Accounting principles

The accounting and valuation principles applied are consistent with the provisions of the Swedish Annual Accounts Act and generally accepted accounting principles (bokföringsnämnden allmänna råd och vägledning).

All amounts are in thousands of Swedish kronor (SEK) unless otherwise stated.

Receivables

Receivables are stated at the amounts estimated to be received, based on individual assessment.

Receivables and payables in foreign currencies

Receivables and payables in foreign currencies are valued at the closing day rate. Where hedging measures have been used, such as forwarding contracts, the agreed exchange rate is applied. Gains and losses relating to operations are accounted for under other financial income and cost.

Bank accounts in foreign currencies

Bank balances in foreign currencies are valued at the closing day rate.

Fixed assets

Tangible fixed assets are stated at their original acquisition values after deduction of depreciation according to plan. Assets are depreciated systematically over their estimated useful lives. The following periods of depreciation are applied: Buildings 5 - 50 years, Radar systems 3 - 20 years and Equipment and tools 1 - 5 years.

Note 2 Associate contributions

The Associates contributed to the operation during the year in accordance with the agreement. The commitments are in local currencies. The received contributions have been accounted in SEK.

	<u>2010</u>
CRIRP (P. R. of China)	2 849
DFG (Germany)	1 732
NIPR (Japan)	1 768
RCN (Norway)	5 745
SA (Finland)	3 371
STFC (United Kingdom)	3 384
VR (Sweden)	5 400
	<u>24 248</u>
Accumulated contributions status as of 2010-12-31	
	<u>1976 - 2010</u>
Previous Associates	190 074
CRIRP (P. R. of China)	13 457
DFG (Germany)	190 480
NIPR (Japan)	68 671
RCN (Norway)	140 121
SA (Finland)	62 188
STFC (United Kingdom)	217 775
VR (Sweden)	113 429
	<u>996 196</u>

Note 3 Personnel costs and average number of employees

The Association employs directly the Headquarters staff, currently about six positions, including the Director. The Headquarters is located in Kiruna, Sweden. The personnel working at the Kiruna (Sweden), Sodankylä (Finland), Svalbard and Tromsö (Norway) sites are not employed by the Association. Instead, the personnel are provided via site contracts by the Swedish Institute of Space Physics (Kiruna site staff), Oulu University (Sodankylä staff) and Tromsö University (Tromsö and Svalbard staff). The Association refunds all expenses related to the provided staff, as well as an additional overhead.

Personnel costs in total

	2010	2009
Salaries and emoluments paid to the Director	1 286	1 240
Other personnel, employed and provided via site contracts	10 971	11 031
Social security contributions amounted to of which for pension costs	4 106	3 944
	2 086	1 992

The Director, Dr. Esa Turunen, started his employment 2009-01-01. His employment contract with Council is for three years.

Of the pension costs, 333 kSEK (320 kSEK) relates to the Director. He and all other directly employed staff are included in ITP like occupational pension plans. For the personnel provided via site contracts, the pension plans are handled by their respective employer.

The members of the board (EISCAT Council) and members of committees, who represents Associates, do not receive remunerations from the Association. Travel expenses in connection with Council and committee meetings are normally covered by the Associates. For the Council Advisory Group, the Association cover meeting and travel costs.

Salaries and emoluments and average number of staff per country

Finland		
Salaries and emoluments	1 029	1 528
Average number of staff - men and women	2 + 0	3 + 0
Norway (including Svalbard)		
Salaries and emoluments	5 818	5 370
Average number of staff - men and women	10 + 0	9 + 0
Sweden		
Salaries and emoluments	5 410	5 372
Average number of staff - men and women	7 + 1	8 + 1

Members of the board and Directors at year-end - men and women

The board consist of delegations from every Associate country each having a Delegate (formal member) and up to two Representatives.

Board members (EISCAT Council)	12 + 4	12 + 4
Directors	1 + 0	1 + 0

Note 4 Own reserves and funds

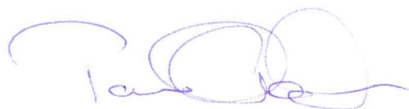
Transactions involving own reserves and funds.

Capital Operating reserve		
Budgeted transfer to the reserve	-884	-1 614
Transfer from the reserve	419	1 469
Investments made	-419	-2 040
External projects reserve		
Project(s) complete, funds released	0	1 504
Restructuring reserve		
Budgeted restructuring costs	0	1 500
Spare parts reserve		
Budgeted transfer to the reserve	-28	-28
Transfer from the reserve	109	9

EISCAT Scientific Association Annual Report 2010

	2010	2009		2010	2009
Investment fund			Note 8 Prepayments and accrued income		
Budgeted transfer to the fund	0	-2 000	The main buildings and systems insurance for 2010 was paid in December. Costs relating to the Antenna III feasibility work were invoiced in February 2011 and the EISCAT_3D_2 project costs spent in 2010 will be claimed from EU in April 2012.		
Surplus fund			Prepaid rents	92	91
Budgeted transfer from the fund	4 196	4 062	Prepaid insurances	139	460
Budgeted transfer to the fund	-2 445	-4 196	Accrued income	462	0
<i>Sum own reserves and funds</i>	<i>949</i>	<i>-1 335</i>	Other items	437	89
Note 5 Appropriations				<u>1 129</u>	<u>640</u>
The outcome for this year became a deficit relative to the budget amounting to -83 kSEK. The deficit was covered by own reserves from the surplus fund. The 2009 outcome resulted in a surplus (3 415 kSEK), which was put in the investment fund.			Note 9 Bank balances status		
Note 6 Transfer from funds invested			Nordea	24 709	19 220
The depreciation cost is covered by funds from Capital - funds invested			Cash in hand	2	2
Note 7 Tangible fixed assets				<u>24 711</u>	<u>19 222</u>
Changes in tangible fixed assets during 2010.			Note 10 Funds invested status		
Buildings			Buildings	3 557	3 843
Opening acquisition value	42 374	42 237	Radar Systems	748	821
Acquisitions during the year	8	137	Equipment and Tools	1 664	2 099
Disposals during the year	0	0		<u>5 968</u>	<u>6 764</u>
Closing acquisition value	42 382	42 374	Note 11 Funds held on reserve		
Opening accumulated depreciation	-38 531	-38 242	Investments were made a bit below the budgeted expectation. More spare parts than budgeted were acquired. Both actions were budget neutral since the differences were covered by reserve transfers. The deficit for this year (-83 kSEK) were taken from the surplus fund. The other transfers were as budgeted.		
Depreciations during the year	-295	-289	Capital operating reserve	1 834	1 369
Disposals during the year	0	0	Equipment repair fund	754	754
Closing accumulated depreciation	-38 825	-38 531	External projects reserve	0	0
Closing residual value	3 557	3 843	Investment fund	7 971	7 971
Radar systems			Restructuring reserve	4 101	4 101
Opening acquisition value	244 484	244 381	Spare parts reserve	290	371
Acquisitions during the year	59	103	Surplus fund	2 362	4 196
Disposals during the year	0	0		<u>17 312</u>	<u>18 763</u>
Closing acquisition value	244 542	244 484	Note 12 Long term liabilities		
Opening accumulated depreciation	-243 662	-242 340	No long term liabilities. The Association is fully funded by the Associates.		
Depreciations during the year	-132	-1 323	Note 13 Liabilities, trade		
Disposals during the year	0	0	The EISCAT_3D_2 preparatory phase project started 2010-10-01. The project is financed by EU's European Commission through the Framework Programme 7 scheme. The contract stipulates that a percentage of the total financing is withheld as contingency and kept in a guarantee fund with the Commission. The first prefinancing, minus the contingency, were received in October. The guarantee fund will be released at the end of the project, 2014-09-30.		
Closing accumulated depreciation	-243 795	-243 662	EISCAT_3D_2 guarantee fund, whole project	2 023	0
Closing residual value	748	821	EISCAT_3D_2 prefinancing, EISCAT share	5 120	0
Equipment and tools			Liabilities, trade	4 282	4 469
Opening acquisition value	33 057	31 925		<u>11 425</u>	<u>4 469</u>
Acquisitions during the year	352	1 229	Note 14 Provisions		
Disposals during the year	-398	-98	None in 2010. In 2009 the provision referred to an erroronus cost debit.		
Closing acquisition value	33 011	33 057	Provisions	0	155
Opening accumulated depreciation	-30 958	-30 283			
Depreciations during the year	-787	-586			
Disposals during the year	398	-89			
Closing accumulated depreciation	-31 347	-30 958			
Closing residual value	1 664	2 099			
<i>Sum tangible fixed assets</i>	<i>5 968</i>	<i>6 764</i>			

Helsinki 2011-05-31



Dr. Tomas Andersson



Dr. Bjørn Jacobsen



Dr. Hiroshi Miyaoka



Dr. Michael Schultz



Dr. Kati Sulonen

Prof. Jian Wu



Dr. Karin Zach



Dr. Esa Turunen
Director

Our audit report was issued on 2011-06-13



Mrs. Annika Wedin
Authorised Public Accountant



Audit report

To the council of EISCAT Scientific Association

Corporate identity number 897300-2549

I have audited the annual accounts, the accounting records and the administration of the council and the director of EISCAT Scientific Association for the year 2010. These accounts and the administration of the association and the application of the Annual Accounts Act when preparing the annual accounts are the responsibility of the council and the director. My responsibility is to express an opinion on the annual accounts and the administration based on my audit.

I conducted my audit in accordance with generally accepted auditing standards in Sweden. Those standards require that I plan and perform the audit to obtain reasonable assurance that the annual accounts are free of material misstatement. An audit includes examining, on a test basis, evidence supporting the amounts and disclosures in the accounts. An audit also includes assessing the accounting principles used and their application by the council and the director and significant estimates made by the council and the director when preparing the annual accounts as well as evaluating the overall presentation of information in the annual accounts. As a basis for my opinion concerning discharge from liability, I examined significant decisions, actions taken and circumstances of the association in order to be able to determine the liability, if any, to the council or the director. I also examined whether any council member or the director has, in any other way, acted in contravention of the Annual Accounts Act or the statutes. I believe that my audit provides a reasonable basis for my opinion set out below.

The annual accounts have been prepared in accordance with the Annual Accounts Act and give a true and fair view of the association's financial position and results of operations in accordance with generally accepted accounting principles in Sweden.

The statutory administration report is consistent with the other parts of the annual accounts.

The council and the director have not acted in contravention of the statutes.

Gävle, 13 June 2011

A handwritten signature in blue ink, appearing to read 'Annika Wedin', is written over a light blue horizontal line.

Annika Wedin
Authorized Public Accountant

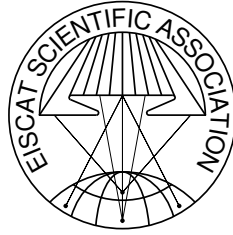
Report 2010 of the EISCAT Scientific Association

©EISCAT Scientific Association

EISCAT Headquarters

Box 812, SE-981 28 Kiruna, Sweden

Scientific contributions: EISCAT Associates and staff



The EISCAT Associates

December 2010

CRIRP

China Research Institute of Radiowave Propagation
China
www.crip.ac.cn

DFG

Deutsche Forschungsgemeinschaft
Germany
www.dfg.de

NERC

Natural Environment Research Council
United Kingdom
www.nerc.ac.uk

NFR

Norges forskningsråd
Norway
www.forskningsradet.no

NIPR

National Institute of Polar Research
Japan
www.nipr.ac.jp

SA

Suomen Akatemia
Finland
www.aka.fi

STEL

Solar Terrestrial Environment Laboratory, Nagoya
Japan
www.stelab.nagoya-u.ac.jp

VR

Vetenskapsrådet
Sweden
www.vr.se

EISCAT Scientific Association

Headquarters

EISCAT Scientific Association
Box 812
SE-981 28 Kiruna, Sweden
Phone: +46 980 79150
Fax: +46 980 79159
www.eiscat.se

Sites

Kiruna

EISCAT Kiruna Site
Box 812
SE-981 28 Kiruna, Sweden
Phone: +46 980 79136
Fax: +46 980 29276

Longyearbyen

EISCAT Svalbard Radar
Postboks 432
N-9171 Longyearbyen, Svalbard
Phone: +47 790 21236
Fax: +47 790 21751

Sodankylä

EISCAT Sodankylä Site
Tähteläntie 54B
FIN-99600 Sodankylä, Finland
Phone: +358 16 619880
Fax: +358 16 610375

Tromsø

EISCAT Tromsø Site
Ramfjordmoen
N-9027 Ramfjordbotn, Norway
Phone: +47 776 20730
Fax: +47 776 20740